The study of transparent hematite films using ultrafast and Raman spectroscopies

by

Sipho Congolo

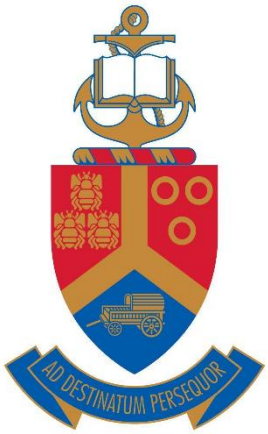

Submitted in partial fulfilment of the requirements

for the degree

***Magister Scientiae* (Physics)**

in the

Faculty of Natural and Agricultural Sciences

Department of Physics

at the

University of Pretoria

November 2019

Supervisor: Prof M.M. Diale

Co-supervisor: Prof. T. P. J. Krüger

Abstract

The study of transparent hematite films using ultrafast and Raman spectroscopies

by

Sipho Congolo

Department of Physics,

University of Pretoria,

Pretoria, 0002, South Africa

Supervisor: Prof Mmantsae M. Diale

Co-supervisor: Prof Tjaart P.J. Krüger

Degree: *Magister Scientiae*

Keywords: Hematite, Spray pyrolysis, Confocal Raman microscopy, Pump-probe Transient absorption spectroscopy

Hematite (Fe_2O_3) is a promising photoanode material that is being studied immensely for its application in solar water splitting to produce hydrogen and oxygen as fuels. It has attractive properties such as a narrow bandgap that allows for absorption of visible light, it is earth-abundant and is an easily processable photocatalytic material. In this study, we report on hematite thin films prepared by spray pyrolysis on fluorine-doped tin oxide (FTO) coated glass substrates. The samples were prepared by spray pyrolysis and treated with tetraethoxysilane as well as post-annealed. We employed ultrafast transient absorption spectroscopy and high-resolution confocal Raman microscopy for analysis of the hematite thin films. For all the films, Raman spectroscopy confirmed the characteristic spectrum of the hematite. The high-resolution Raman mapping showed a uniform intensity over the analyzed areas which suggests a uniform coating of the hematite films on the FTO substrates. Ultrafast transient absorption spectroscopy was used to investigate the effect of three experimental parameters; the effect of the spray volume, tetraethoxysilicate treatment of the hematite and post-annealing at 500 ºC for 2 hours with 10 ºC/min ramping. All three parameters gave a positive result. Ultrafast transient absorption spectroscopy indicates that all three experimental parameters slowed down electron-hole recombination. Global analysis of the difference absorption data resolved the spectra and associated decay lifetimes of three distinct processes, operating on the ultrafast, tens of picoseconds and hundreds of picoseconds timescales. Thus, understanding these properties will aid in the engineering of this material to prolong recombination and, as a result, improve its solar to hydrogen conversion efficiency in photoelectrochemical cells.

Declaration of originality

I, *Sipho Congolo*, declare that the dissertation, which I hereby submit for the degree *Magister Scientiae* in *Physics* at the *University of Pretoria*, is my own work and has not previously been submitted by me for a degree at this or any other tertiary institution.

Signature: ……

Sipho Congolo

Student number: **12047857**

Date: ……

Dedication

I dedicate this dissertation to the memory of my late best friend and colleague**, Kamohelo Samuel Matshoba**, may his soul rest in peace.

Acknowledgments

I would like to express my deepest and most sincere gratitude to the following people whom have made an appreciable contribution to this dissertation:

- Firstly, to my supervisor Prof M.M Diale for the support, patience and guidance throughout my studies.
- My co-supervisor Prof. T. P. J. Krüger for all the technical assistance and guidance.
- To my colleagues, Asmita Singh, Moshawe J. Madito, Alexander T. Paradzah, Huzifa M.A.M. Elnour and Arthur J. Harrison who were very helpful, kind and patient with me during my experimental work.
- My closest friends Ndivhuwo Ratshikakala, Thapelo Mokgadi and Thokozani Mlotshwa whom encouraged me to persevere even when I wanted to give up.
- University of Pretoria Physics Department leadership, staff and fellow students
- Above all else my mother Sanah Congolo and siblings who kept me strong and supported me throughout my life's journey.
- Lastly, I thank God almighty!

Financial Assistance

Financial assistance provided by the National Research Foundation (NRF)[1] in respect of the costs of the study, is hereby acknowledged. Opinions or conclusions that have been expressed in this study are those of the writer and must not be seen to represent the views, opinions, or conclusions of the NRF.

[1] Disclaimer: Any opinions, findings and conclusions or recommendations in this material are those of the author(s) and therefore the NRF do not accept any liability in regard thereto.

List of Abbreviation and Acronyms

α-Fe_2O_3	Hematite
ΔA	Difference Absorption
OD	Optical density
GSB	Ground state bleach
ESA	Excited state absorption
SE	Stimulated emission
TAS	Transient Absorption Spectroscopy
EADS	Evolution associated difference spectra
DADS	Decay associated difference spectra
SADS	Species associated difference spectra
PEC	Photoelectrochemical cell
TEOS	Tetraethoxysilane
FTO	Fluorine-doped tin oxide
FWHM	Full Width at Half Maximum
AFM	Atomic Force Microscopy

List of Figures

Contents

CHAPTER 1

Introduction

1.1 Global Energy Challenge

About three hundred years ago, people used wood as their main energy source, then started slowly moving on to coal, oil, natural gas. In the past 10 years the energy sector has shifted more towards nuclear energy and renewable energies. Energy is vital to human life and the sustainability of our existence as we know it. Energy sources have changed vastly over time continuously redrawing the world map of key energy countries i.e. the world's largest producer of electricity from renewable sources. The world is currently facing many challenges with regards to energy production and its effect on the environment. The world energy consumption, mainly in fossil fuels, is continuously rising, as shown in figure 1.1, due to an ever increasing human population as well as economic development. Subsequently, this rise can be attributed to increasing industries and advanced technologies that place a huge demand on energy.

Figure 1.1 shows that the energy consumption of fossil fuels, namely coal, oil and natural gas, has approximately tripled from the years 1965 to 2015. Thus, apart from the harmful emissions, these energy sources are steadily being depleted from the earth. Although fossil fuels are continually being formed via natural processes, they take a vast amount of time to form and are being consumed at a much faster rate than new ones can form. Meanwhile, the energy consumption through nuclear and renewable energy have also steadily increased but less than that of fossil fuel, seeing a slight increase of renewable energies from the years 2005 to 2015.

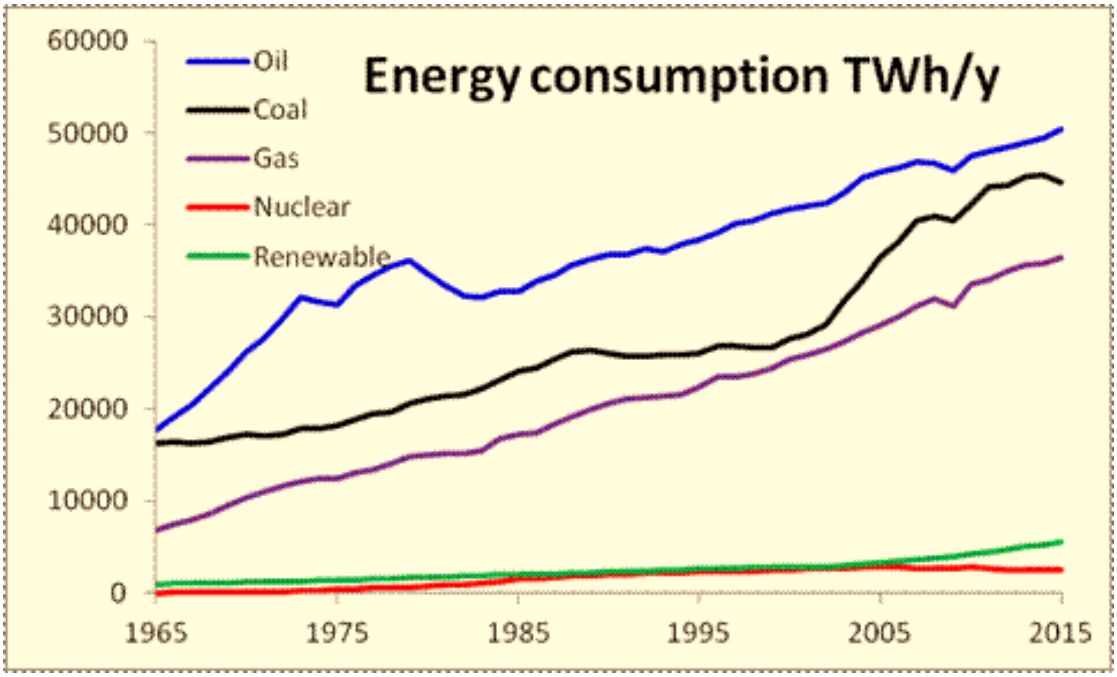

Figure 1.1. A graph of the world energy consumption per year from 1965-2015 [1].

With the continuous use of fossil fuels many challenges have arisen which severely impact our environment and henceforth our wellbeing. One of the challenges that has received much attention over the years is the greenhouse effect, depicted in figure 1.2, which changes the earth's climate. The greenhouse effect is a naturally occurring process that heats the earth's surface. When solar energy reaches the earth's atmosphere some of it is reflected and some of it is trapped and re-radiated by greenhouse gases. These gases include carbon dioxide (CO_2), water vapour, methane, nitrous oxide, ozone and some artificial chemicals like chlorofluorocarbons (CFCs). These gases trap extra heat and, as a result, cause the earth's temperature to rise. This in turn leads to disasters such as flooding due to rising sea levels and acid rain which is destroying forests. Recent news from Australia has reported the death of fish in oceans due to global warming [2].

In addition to the harmful effects of non-renewable energy sources the world is currently facing an energy crisis. In 2014 the world energy consumption was estimated to 155 481 terawatt-hour (TWh) and is estimated to double by 2060 [3].

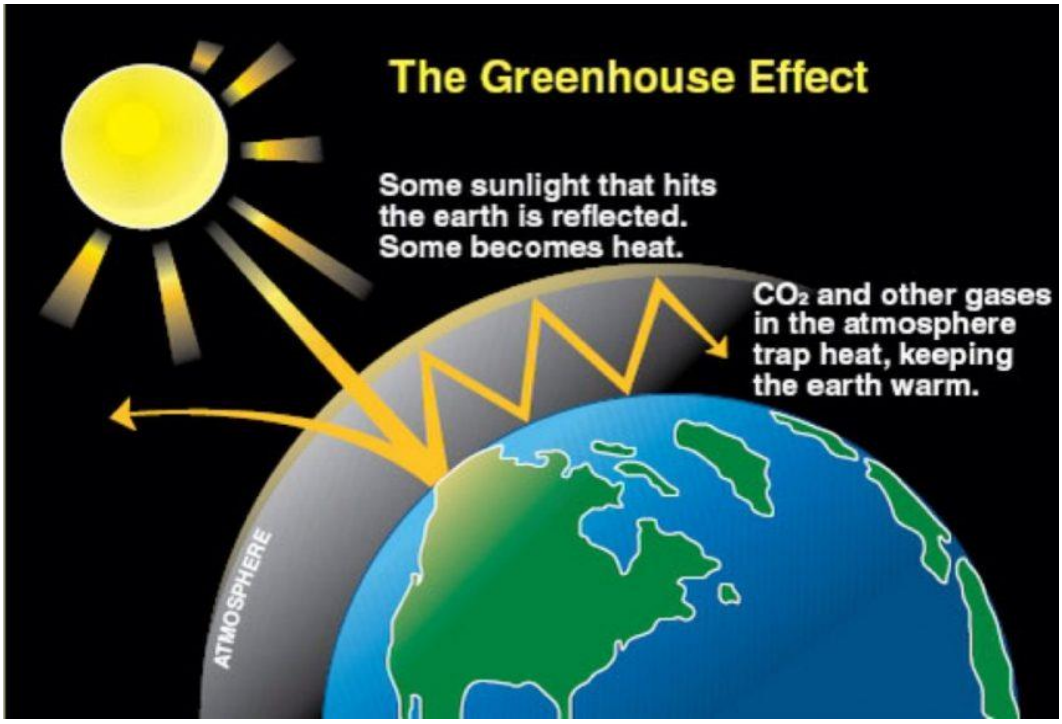

Figure 1.2. A depiction of the greenhouse effect [2].

Considering the current energy crisis South Africa is facing with our major electricity supplier, Eskom, struggling to generate and supply our country with enough power to meet the needs of the citizens, other avenues of alternative energy production need to be made available. With an increase in population and a growing economy the demand for energy will continue to rise and will inevitably place a huge strain on the supply of electricity if other alternatives are not explored.

1.2 Solar Energy

Solar energy has over the years received a lot of publicity among the renewable energy sources due to its relatively easy methods of collection and its abundance. The sun is a fusion reactor that has presumably been burning over billions of years. The earth receives an enormous amount of solar energy and essentially 100% of the energy that we use for consumption comes from the sun. Of the solar energy coming into the earth, on average, 6% is scattered from the atmosphere, 20% is scattered and reflected by clouds, 19% is absorbed by the atmosphere and clouds, 4% is reflected by earth's surface and 51% is absorbed by the earth (land and oceans) as shown in figure 1.3 [2] . The sun supplies enough energy in one minute to sustain the world's energy needs for a whole year and in one day it provides more energy than our current population can consume in 27 years [4].

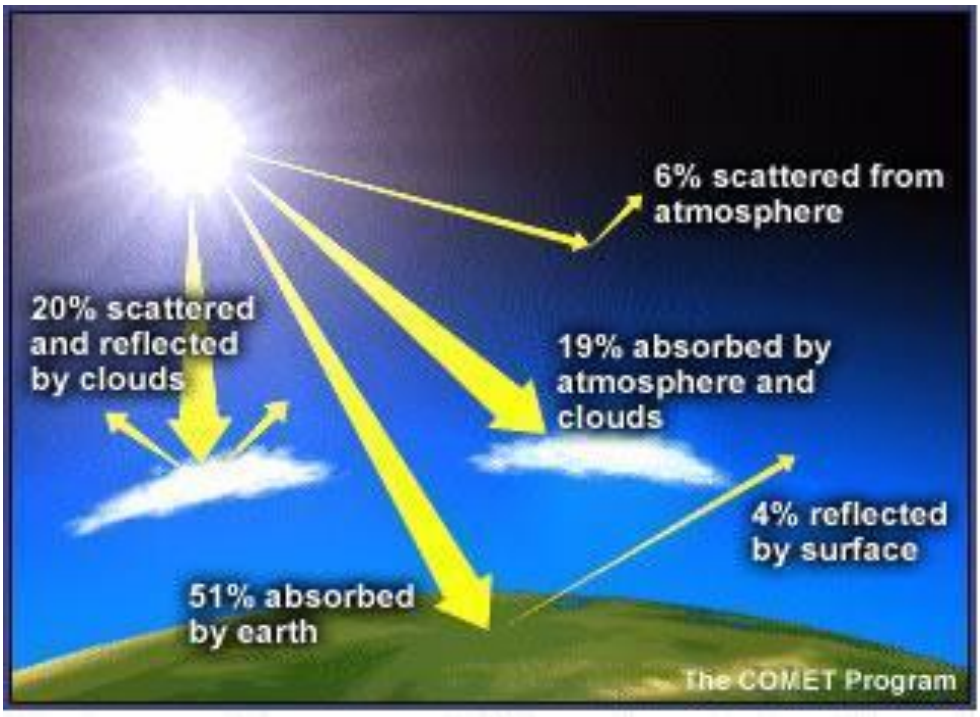

Figure 1.3. Depiction of the amount solar energy, broken down into percentages, that is used by the earth [5].

However, the main problem is the conversion and storage of this solar energy. Research has been focused on developing materials that can be used in technologies that efficiently convert solar energy to electrical energy. Photovoltaics are technologies that directly convert light into electricity at the atomic level. The silicon solar cell, often referred to as 1st generation panels, currently dominates 90% of the solar cell market. When solar energy is incident on the solar cell, electrons are released from the atoms in the semiconductor material. If electrical conductors are attached to the positive and negative terminals, forming a complete electrical circuit, the electrons generate an electric current i.e. electricity.

Photosynthesis is a naturally occurring process in plants, algae and certain bacteria that efficiently converts solar energy into chemical energy as shown in figure 1.4. The science community has been trying to mimic this process by using materials such as semiconductor metal oxides that absorb visible light to generate electron-hole pairs. This process is possible due to the photovoltaic effect [6]. Solar energy can only be used while the sun is up, therefore once the sun sets the issue of solar energy storage arises.

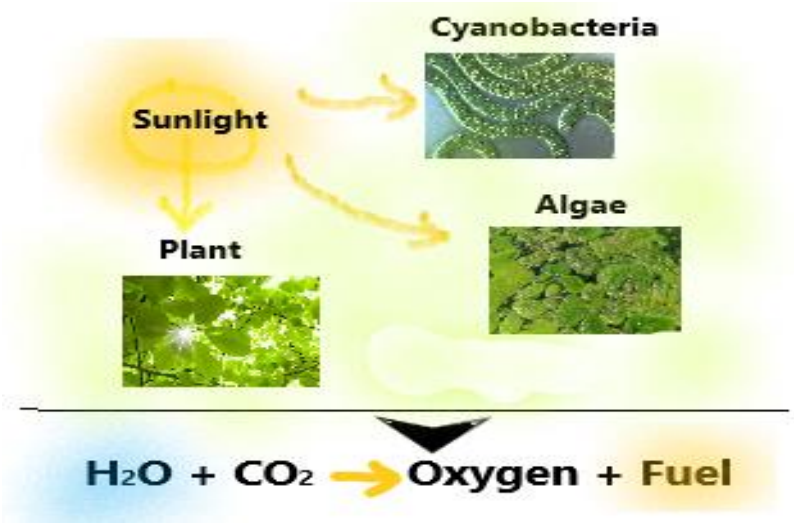

Figure 1.4. Depiction of natural photosynthesis where sunlight is used by plants to convert water and carbon dioxide into oxygen and fuel [7].

Traditionally batteries such as the lithium-ion battery shown in figure 1.5 are used as energy storing devices. These batteries contain two electrodes - an anode and a cathode - separated by an electrolyte such as a liquid or gel containing ions and two current collectors, positive and negative terminals. The anode and cathode store the lithium. Positively charged lithium ions move from the anode to the cathode through the electrolyte and can also move in the opposite direction. Free electrons are generated at the anode by the movement of lithium ions which create a charge at the positive current collector. An electrical current then flows from the positive terminal through a device being powered to the negative current collector as shown in figure 1.5. The energy density of a battery is the amount of energy a battery can store with respect to its mass which is measured in watts-hour per kilogram. The power density of a battery is the amount of power that can be generated with respect to the battery's mass which is measured in watts per kilogram [8]. Using large lithium-ion batteries as storage is not economically and environmentally friendly. Furthermore, these batteries can only store energy for a certain amount of time because once the charging source is removed, they start to discharge.

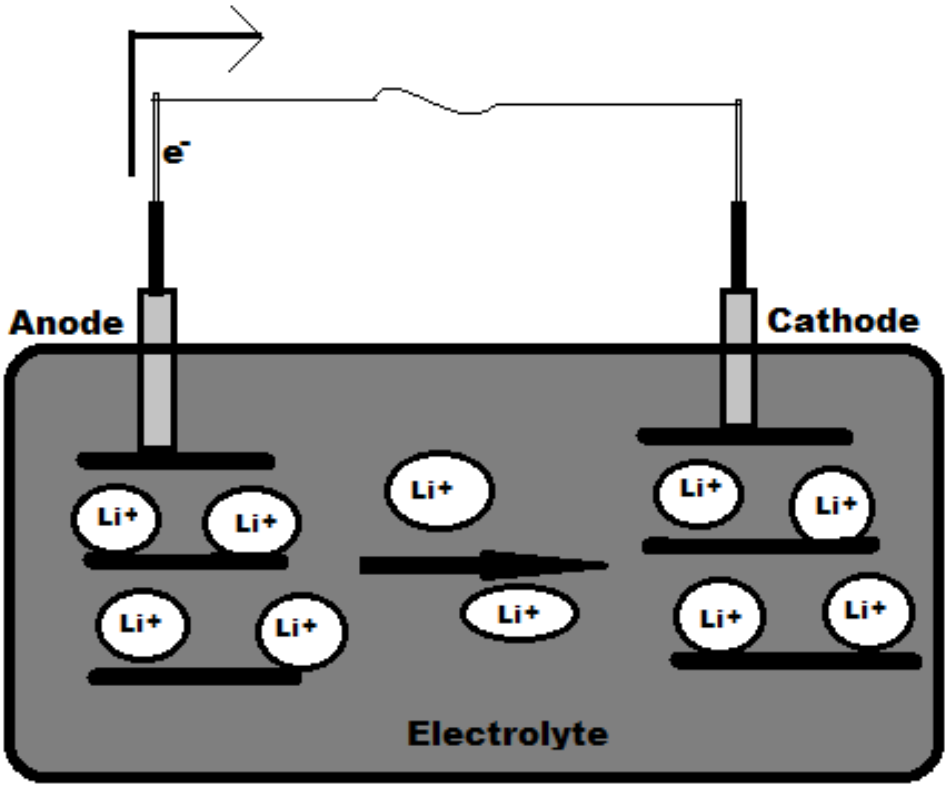

Figure 1.5. A schematic diagram of a lithium ion battery [9].

A solution to this problem would be to find alternative ways to store solar energy by mimicking natural photosynthesis.

Solar water splitting is an artificial photosynthetic process that chemically dissociates water into its constituents, hydrogen (H_2) and oxygen (O_2), using sunlight. In theory only three things are needed for this process to occur, viz. photons, water and a catalyst [10]. To produce hydrogen and oxygen efficiently this process would have to be operating at a very low cost. One could dissociate water into these elements at very high efficiencies if cost did not matter at all. The high efficiency tandem solar cells and an electrolyzer operating at high faradaic efficiency would make this possible; however, cost does matter, and these technologies would be extremely costly. Thus, to achieve solar water splitting at high efficiencies a semiconductor material is needed capable of visible light absorption, separation of photogenerated carriers as

well as to produce H_2 and O_2 from water directly in one cost-effective technology. Furthermore, the material needs to be stable under aqueous environments to avoid degradation, it must be abundant and have a suitable bandgap for sufficient reduction of hydrogen and oxidation of oxygen from water [11].

1.3 Solar water splitting

Photoelectrochemical water splitting was first demonstrated by Fujishima and Honda [11] using a rutile (TiO_2) crystal as the photoanode and platinum as the counter-electrode (figure 1.6). When incident light interacts with the photoanode an electron (e^-)-hole (h^+) pair is generated. Thereafter the holes oxidize the water at the photoanode (TiO_2) surface to produce oxygen and the electrons flow to the platinum counter-electrode where water is reduced to form hydrogen. The oxidation of water by holes is given by the equation:

$$H_2O + 2h^+ \rightarrow 2H^+ + \tfrac{1}{2}O_2 \quad E^0_{ox} = -1.23V\ vs.NHE \tag{1.1}$$

where NHE is the normal hydrogen electrode defined as the potential of a platinum electrode in 1 M acid solution. The photogenerated electrons migrate to the counter-electrode under an applied voltage between the two electrodes where hydrogen ions (H^+) are reduced to hydrogen gas (H_2), as given by the equation:

$$2H^+ + 2e^- \rightarrow H_2,\ E^0_{red} = 0V\ vs.NHE \tag{1.2}$$

The overall equation for this process is:

$$2H_2O \rightarrow 2H_2 + O_2, \tag{1.3}$$

where equations (1.1) and (1.2) are the two half equations of water splitting with the voltage corresponding to a pH of 0. Honda and Fujishima showed in 1972 that water splitting was possible with TiO_2 and since then its photoanodic properties have been widely investigated.

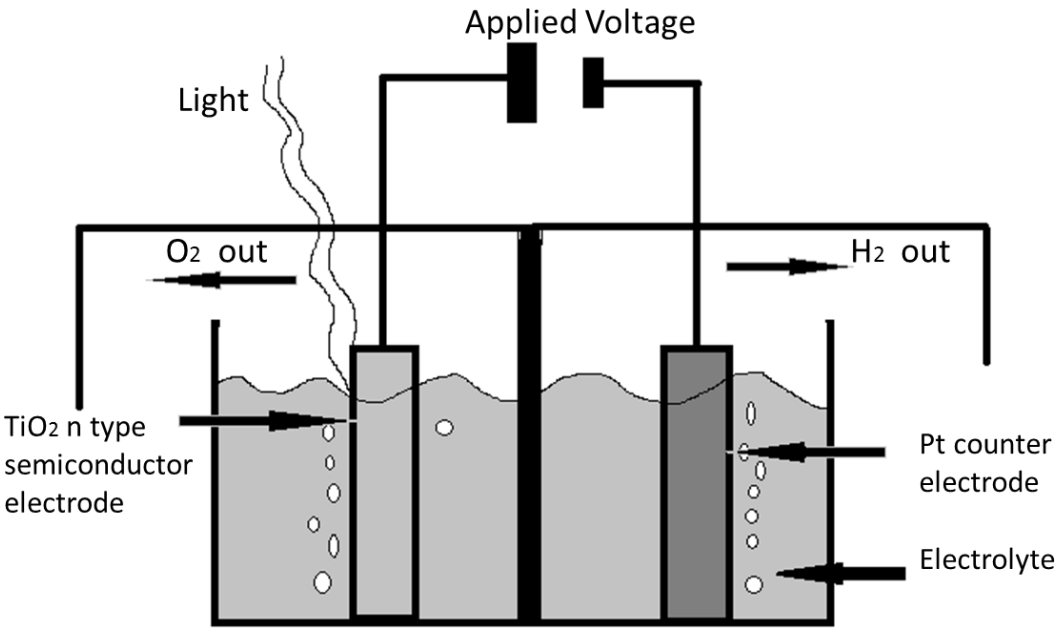

Figure 1.6. A schematic of the photoelectrochemical cell used by Honda and Fujishima to demonstrate solar water splitting [11].

TiO_2 was particularly attractive because of its abundance, high resistance to photocorrosion, nontoxicity and its relatively low cost [12]. Although TiO_2 is stable when illuminated under aqueous conditions, it has a large band gap (~3.0 eV) which hinders its ability to absorb light optimally as it is limited to the UV portion of the solar spectrum and thus limits its maximum efficiency. For an ideal semiconductor to be used as a photoelectrode the band gap should be >1.23 eV. This is because in order to achieve photocatalytic water splitting using a single photocatalyst, the band gap of the semiconductor must straddle the reduction and oxidation potentials of water, which are +0 and +1.23 V vs. normal hydrogen electrode (NHE), respectively, when the reactant solution is at pH 0, as shown in figure 1.7. This is the one-step water-splitting principle [13].

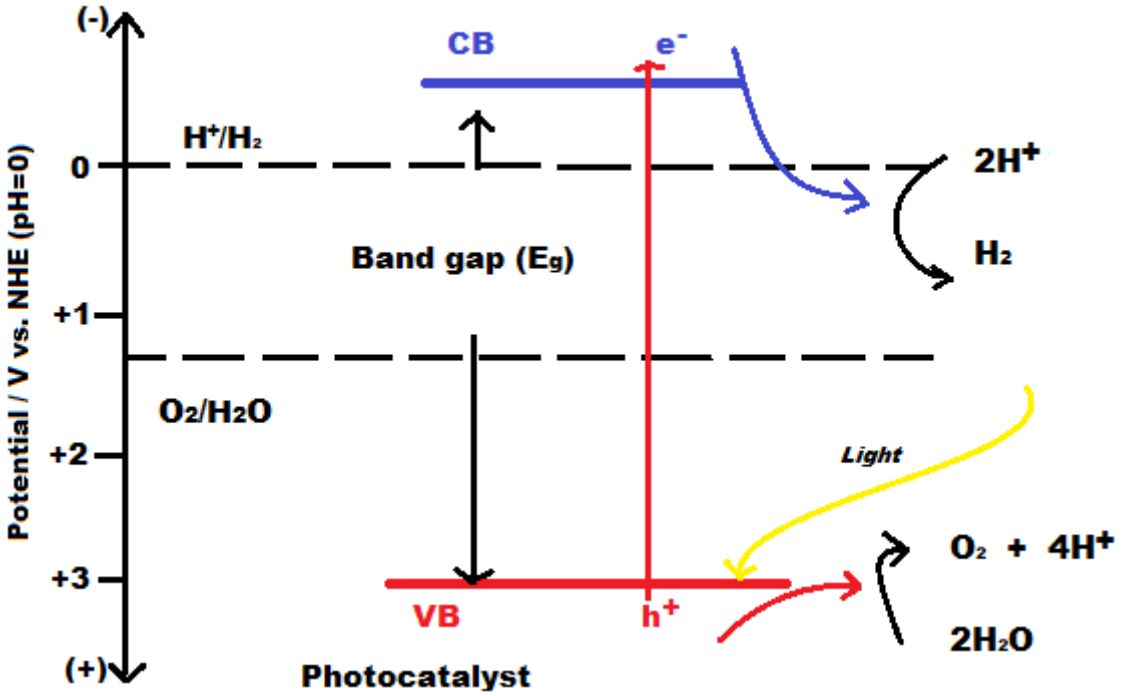

Figure 1.7. Schematic energy diagrams of photocatalytic water splitting based on one step excitation where is the conduction band (CB) is at apotential of +0 V and the valence band (VB) is at +1.23V [14].

There are many materials that satisfy these conditions such as GaP, Nb_2O_5, CdS, and $SrTiO_3$. However, most of these semiconductors are not suitable to be used either due to their wide band gap, instability in an aqueous electrolyte or photocorrosive nature [15][16].

Metal oxides have been widely investigated and have shown potential to be used as photoelectrodes mainly due to their stability in aqueous environments. Some of these metal oxides are Fe_2O_3, $BiVO_4$, and CdO. Although most of these materials are not capable of hydrogen production due to their conduction band edge being lower than the hydrogen production potential (figure 1.8), their valence band edge is well placed for oxygen production. A two-electrode setup will aid in the hydrogen production with the reduction of H^+ to H_2 occurring at the counter-electrode.

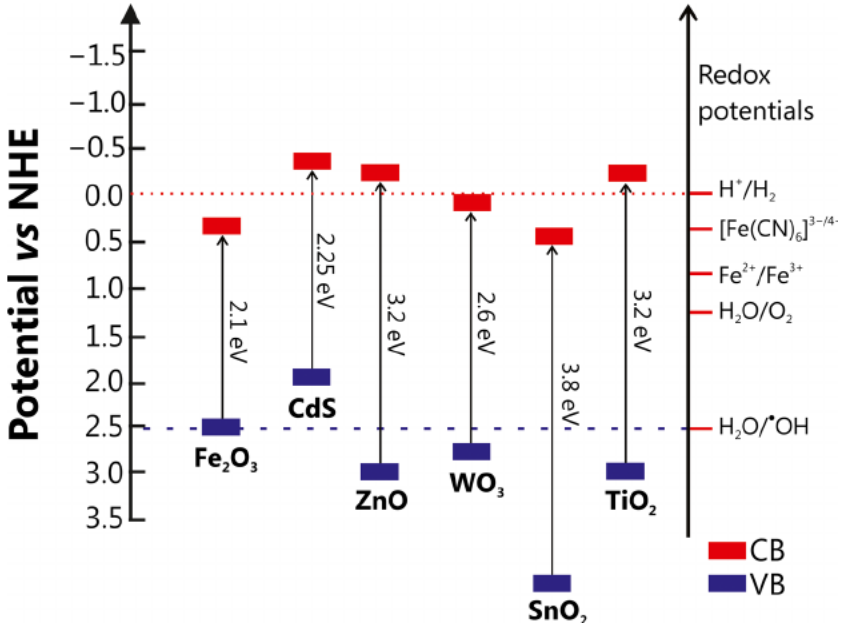

Figure 1.8. Energy positions of conduction band (CB) and valence band (VB) of selected solar cells used in photoelectrocatalysis [17].

In this work we investigated hematite (α-Fe_2O_3) as photoanode material. Hematite has been under scrutiny due to its non-toxicity, abundance, stability in aqueous solutions and photo-activeness under visible light. The material has a small band gap (~2.1 eV) that permits optimal visible light absorption and a 15.3% theoretical solar to hydrogen conversion efficiency or 12.6 mA/cm^2 at 1.23 V versus reversible hydrogen electrode/reference electrode (RHE) under 1-sun irradiation photocurrent generation [16][18]. However, this material has a few shortcomings, namely short hole diffusion length (2–4 nm) and poor conductivity, which lead to very fast electron-hole pair recombination [19]. Various methods have been employed to suppress *e-h* recombination such as doping or the use of underlayers. In subsequent chapters of the study, we present a few methods to suppress recombination and characterize the samples using ultrafast transient absorption (TA) spectroscopy and confocal Raman microscopy.

1.4 Aims and Objectives

Despite the current advancements for achieving a high solar to hydrogen conversion efficiency in PEC water splitting, finding a good semiconductor to use as a photoanode in PECs remains a challenge. This study is aimed at investigating and improving the optical properties of transparent nanoparticle hematite thin films prepared by spray pyrolysis using confocal Raman microscopy and ultrafast spectroscopy.

The objectives of this study are:

I. Using high resolution confocal Raman microscopy to study the morphology of the as prepared samples.

II. Using ultrafast pump probe transient absorption spectroscopy to carry out a lifetime study and to obtain the absorption spectra of the transient states and the number of intermediate states with distinct lifetimes of photogenerated charge carriers.

1.5 Dissertation outline

The main purpose of this work was conducting a transient lifetime study of the photoexcited electron-hole pairs in hematite thin films. Transient lifetime measurements rely on the decay of carriers over time. Carriers are generated by a very short pulse of light and the decay of the carrier density with time is measured. Generally, the longer the minority carrier lifetime the more slowly the carriers decay. Chapter 2 gives a detailed description of hematite in terms of its chemical and optical properties to elucidate its function as a photoanode in PECs. Since hematite was prepared using spray pyrolysis and using three separate experimental parameters. Chapter 3 explains the techniques employed to analyse these samples. Confocal Raman microscopy was used to study the morphology of the nanostructured thin films and ultrafast transient absorption spectroscopy to study the electron-hole recombination rates, the absorption

spectra of the transient states and the number of intermediate states with distinct lifetimes. Chapter 4 presents the results and discussion of the experiments. A broad summary of the results is presented in this dissertation as well as prospects for future work are given in Chapter 6.

CHAPTER 2

Hematite as a photoanode

Introduction

In this chapter, we will discuss the origins of hematite and the work that has been done on it as a photoanode. The aim is to understand the basic properties of this material, how they can be enhanced to improve its efficiency and why among other materials it is a suitable candidate to be used as a photoelectrode for solar water splitting.

2.1 Origins of Hematite

Iron oxides are generally classified as rust, especially when the iron oxide forms in wet or humid conditions. Thus, this needs to be taken into account when the material is placed in a photoelectrochemical cell environment. Hematite, an iron (III) oxide (α-Fe_2O_3) mineral, is one of many and the oldest of the known mineral iron oxides and is just one of the many phases of iron oxide. It has a reddish-brown colour, sometimes black or silver-grey as shown in figure 2.3 [20]. The mineral is mined as the main ore of iron where it is abundant. Its colour also allows it to be used as a pigment. Furthermore, hematite has many applications in industry such as jewellery and art. The material has also received attention mostly for its ability to serve as a photoanode semiconductor for solar water splitting in photoelectrochemical cells.

Figure 2.1. A specimen of massive hematite about ten centimeters long [21].

2.2 Hematite

One major challenge with PEC technology is finding a good semiconductor material to be used as a photoanode. In semiconducting materials for PEC cells, research efforts on hematite (α-Fe_2O_3) films have been focused on substituting anatase (TiO_2) which absorbs visible light poorly because of a large energy band gap (~ 3.2 eV) [22]. α-Fe_2O_3 has over the years received much publicity as a potential applicant with a high theoretical maximum efficiency of 12.9% [23]. Iron compounds generally are biocompatible and environmentally friendly [24]. Moreover, small iron oxides and hematite materials have a low per unit cost. Hematite used as a photoanode in PECs was first reported by Bard and Hardee [25]. They found the material to be stable in neutral and basic electrolytes when placed in PEC operating conditions. Additional attributes in favour of this electrochemically stable compound are its relative abundance, low production cost and non-toxicity [26], [27]. However, in light of its attractive attributes this material has a few limitations: its low conductivity and exceptional short hole diffusion length (2–4 nm) impede charge transport and limit the efficiency. As a result, these limitations lead to a high recombination rate of photogenerated charge carriers [18], [19]. To

address these shortcomings, scientists have tried surface treatment of hematite which has shown to have improved the material's properties. Methods such as synthesis of nanostructured hematite including nanowires and nanorods [28], [29], incorporation of host-guest heterostructures [30], elemental doping and heat treatment [18], [31]–[33] have been employed.

2.3 Electronic Structure

Hematite (α-Fe_2O_3) is isostructural with corundum (α-Al_2O_3) structure having a hexagonal cell based on anion hcp packing (figure 2.4) and a narrow bandgap (1.9 -2.3 eV), which allows for absorption of ~40% in the visible region of the solar spectrum [34], [35]. The material has optical absorption bands located in the ultraviolet and near-infrared regions as a result of charge transfer transitions and crystal field [36]. A broad-band absorption of 400-600 nm due to ligand-to-metal charge transfer is observed at 400 nm coupled with pair excitation processes at 485-500 nm [37]. In nanosized α-Fe_2O_3 particles it has been observed that the relative intensities of different spectral regions can change due to particle size. This is attributed to the enhanced pair excitation in larger particles along with a redshift of the charge transfer transitions [38]. The electronic structure of α-Fe_2O_3 contains an empty conduction band with Fe 3d character and a valence band emanating from Fe 3d($2t_{2g}$) and O 2p orbitals [39]. The electronic structure of hematite as a photoanode can be influenced when it comes into contact with an aqueous electrolyte in a PEC. Even without an applied voltage, a chemically induced surface potential can occur.

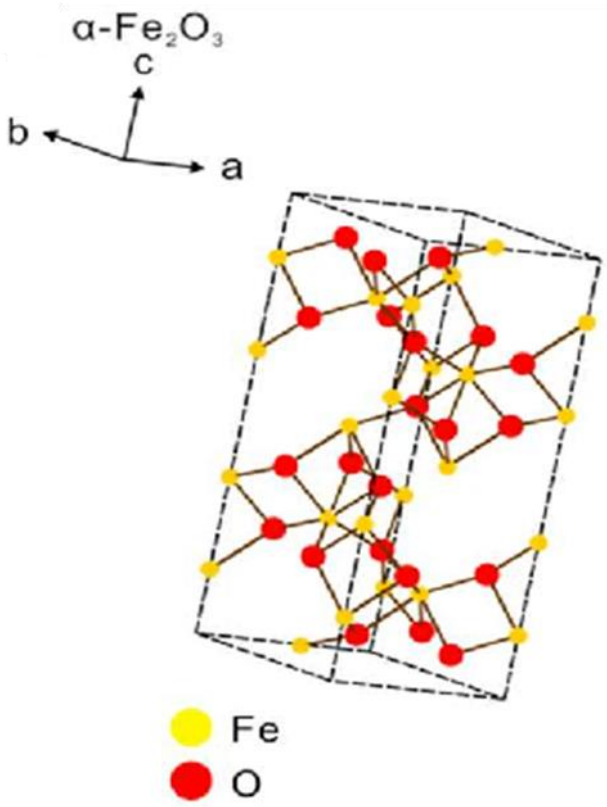

Figure 2.2. Schematic diagram of isostructural α-Fe2O3 having a hexagonal cell based on anion hcp packing [40].

2.4 Synthesis of hematite

There are many studies in literature that address different preparation methods of hematite. These include atomic layer deposition (ALD) of which, when annealing the ultrathin film hematite at 800°C, substantially improves the water oxidation efficiency, electrodeposition (ED), elemental doping (i.e. Ti, Pt etc.), integration of thin underlayers (electron collectors), polymeric precursor method (Pechini) and spray pyrolysis [23], [27], [41], [42]. Chemical spray pyrolysis is a low cost, simple and versatile method and can be used for the preparation of many different types of thin films. The method also allows for doping where the dopant concentration can very accurately be determined [43]. Satsangia et al. reported that a thin film of hematite prepared by spray pyrolysis, which had a particle size of 20–30 nm, exhibited better

photoresponse as compared to the films prepared by sol–gel methods [44]. Studies of hematite prepared by spray pyrolysis are very limited as there are several methods that can be employed in the preparation of mesoscopic hematite films. Spray pyrolysis is a versatile method that can be varied and improved and it has been shown in literature that films prepared by ultrasonic spray pyrolysis (USP) allow for better light harvesting than those prepared by conventional spray pyrolysis [45]. In this work we have used a home-made spray pyrolysis setup.

Bagheri and co-workers synthesized nanocrystalline α-Fe_2O_3 powder, using gelatine as a polymerizing agent, by a sol-gel route in a simple, ecofriendly and cost effective way [46]. This was achieved by using iron nitrate as an iron source and gelatine as stabilizer and gelling agent to reduce the agglomeration of nanoparticles. In this process iron nitrate and gelatine are dissolved in distilled water separately then the two solutions are mixed carefully and the resulting solution turns into a gel after sufficient stirring. The obtained compound was calcined at 600°C using a muffle furnace. X-ray diffraction (XRD) was used to determine the crystal phase identification and crystallite size. Scanning electron microscope (SEM) and transmission electron microscopy (TEM) were used to determine the morphology and particle size of the as-prepare α-Fe_2O_3. FTIR spectroscopy was employed to give qualitative information about the way in which the adsorbed molecules are bonded to the surface as well as the structural information of the hematite. It was found that the particles of the produced α-Fe_2O_3 were approximately 30–40 nm in size. SEM and TEM analysis showed that the material was highly crystallized in the range of 30–40 nm and the particles were spherical in shape. Thus, sol-gel chemistry is a versatile tool for both the preparation and understanding of catalytic materials.

Over the years, electrochemical methods have sparked an interest in the synthesis of nanosized metal oxide powder and films due to its simplicity and low temperature operations. Chandrappa and Venkatesha [47] have successfully synthesised α-Fe_2O_3 using the hybrid electrochemical-thermal method. This process happened in electrolysis. Millipore water was used to prepare the electrolyte solution. Three different concentrations of sodium bicarbonate ($NaHCO_3$), 30, 60 and 120 mM were prepared in the Millipore water where the pH was kept at 8.5 for each electrolyte solution. The anode and cathode were both iron plates that were placed inside the electrolyte. The iron plates were immersed in dilute hydrochloric acid, of 1M concentration, for activation purposes. During the electrolysis process bluish black particles were formed in the solution and finally turned to brown particles. The pH rose and reached a maximum of 10.5 during this process. The brown particles were filtered and separated from the solution. The resulting particles were then calcined at different temperatures from as low as 60 °C to a maximum of 900 °C for 1 h. XRD was used for phase analysis and to determine the crystal size. SEM was employed for morphology and compositional analysis. TEM study was carried out on the samples to ensure that the size of α-Fe_2O_3 particles were in the nanometer range. The UV–Visible spectra were recorded for the analysis of the optical properties of the nanoparticles. The nanoparticles were dipped in ethanol and sonicated before the UV–Visible measurement were taken for uniform dispersion. The Debye–Scherrer equation, $D = \frac{K\lambda}{\beta \cos\theta}$, was used to calculate the average crystallite sizes where D is the diameter of the crystallite size, λ the wavelength of incident beam, β the broadening of the diffraction line measured in radians at half of its maximum intensity (FWHM), K the shape factor (the typical value is 0.9), and θ is the Bragg angle.

Li and his co-workers [48] prepared hematite nanocrystals with amorphous iron oxide layers by hydrothermal conditions. This was achieved by hydrothermal reactions of 0.25 M ferric nitrate solutions in 15 ml stainless steel autoclaves. $Fe(NO_3)_3 \cdot 9H_2O$ reagent was used as the starting material. The $Fe(NO_3)_3$ aqueous solution was charged into an autoclave halfway full by volume. The autoclave was sealed and submerged into a molten salt bath at a specific temperature for a given time period. The autoclaves were cooled in air after the reactions had taken place then dried in an oven at 50˚C. The finding of this work yielded a better understanding of the direct formation of magnetic nanocomposites by hydrothermal conditions.

A study by Hu et al. [49] reports on the preparation of α-Fe_2O_3 snowflake hierarchical structures on a large scale in an efficient microwave-assisted hydrothermal process. The synthesis of α-Fe_2O_3 using this method was reported as a fast and economical process and takes advantage of microwave irradiation and hydrothermal effects. Unlike the solution-phase synthetic method that uses conventional heating [50], microwave irradiation causes a faster reaction due to the interaction of microwave field with reactant molecules. Furthermore, this process has the potential for scale-up industrial production. The synthesis of α-Fe_2O_3 snowflake hierarchical structures involves sealing 30 mL of an aqueous potassium ferricyanide ($K_3[Fe(CN)_6]$) solution in a Teflon-lined double-walled digestion vessel. The mixture is treated in a microwave digestion system at a controlled temperature. A temperature probe was fitted to the reaction vessel. The vessel is then cooled to room temperature and the product was collected, washed with deionized water and absolute ethanol. XRD measurements showed that the product was crystalline. Raman spectroscopy was used to confirm the characteristics peaks of hematite phase. The surface electronic states and the chemical composition of the product were examined by using X-ray photoelectron spectroscopy (XPS) and SEM was used to study the morphology of the products.

2.5 Doping enhancements and surface treatment of pristine hematite

Often hematite nanocrystals are used to prepare photoanodes in a working PEC for photooxidation of water. However, due to the low efficiency of the material a lot of work has been devoted to the enhancement of its properties. Elemental doping and surface treatment are among the few methods that have been employed for this cause. Titanium has shown to be a good dopant in hematite thin films prepared by deposition annealing using titanium butoxide ($C_{16}H_{36}O_4Ti$) and $FeCl_3$ as precursors [51]. After doping the material with Ti the photocurrent density increased from 1.83 mA cm^{-2} *vs.* RHE to 3 mA cm^{-2}. It was also observed that the electron-hole pair recombination reduced due to an increase in donor density. Therefore, this led to a high photocurrent density. Hematite can also be doped with tin using SnO_2 as a precursor and the particle size of tin-doped hematite can be controlled by changing the post-deposition annealing conditions and also varying the precursor composition [52]. Si doping is also an effective way to increase the efficiency of hematite. Kennedy [53] obtained a photocurrent density of 140 μA cm^{-2} at 2 atom% Si through preparing Si-doped hematite films. The films were prepared by pressing and sintering (at 1250 °C to 1350 °C for 4 hours) of hematite and silicon oxide powders. By treating the material with 1M of KI solution the photoresponse was improved and consequently improving the photocurrent by a factor of 3. Other elements such as Cd, Ni, Pt, Cr, Mo, Zr and Ge have been studied as dopants to increase the efficiency of hematite films. Surface treatment is another approach in addition to doping of increasing the efficiency of hematite thin films. Two approaches that have been investigated are the overlayer and underlayer approach. Hematite ultrathin films have been overlaid with group 13 oxides which showed to improve the photocurrent of the onset potential by up to 200mV for water oxidation [54]. Host (or underlayer material) has also shown to significantly improve the efficiency of hematite in water oxidation. The host material increases the

photocurrent density through diffusion doping and reduces recombination of electrons at the fluorine-doped tin oxide (FTO)/Hematite interface. This in turn increases the hole lifetimes [55], [56]. Heat treatment (annealing) is one other form of surface treatment that has proven to increase the crystallinity of hematite as well as the photocurrent [57].

The measured activation energy E_a for hematite is ~1.0 eV, between 450°C and 800°C, which accounts for both carrier formation and hopping mobility. Thus, the presence of impurities or defects decreases E_a to ~0.1 eV and below temperatures of 450°C E_a is ~0.7 eV due to grain boundaries or surface effects [58]. Doping generally results in an effect on the conductivity by changing carrier concentrations and/or carrier mobility. Liao et al. reported on electron transport in pure and doped hematite. The study was carried out by using quantum mechanics to understand how titanium, zirconium, silicon, or germanium n-type doping affects the electron transport mechanism in hematite. Their results suggest that the doping of hematite with silicon, zirconium or germanium is better than titanium doping due to the fact that the former dopants do not act as electron trapping sites. This is because Zr(III) has a higher instability level than Ti(III) and silicon has more covalent interactions with oxygen. Therefore, the use of n-type dopants that easily ionize completely or promote covalent bonds to oxygen can provide more charge carriers while not preventing charge transport [58].

Zhou et al. [17] employed spin-polarized density functional theory with the on-site Coulomb correction (DFT+U) to study the doping of hematite with group IV elements, i.e., Si, Ge, and Sn. Three important conclusions were deduced from the formation energies and chemical potentials that were calculated: low oxygen pressure is favoured for doping both substitutional and interstitial dopants, substitutional doping of the Fe atom at the lattice site is more stable than interstitial doping in the octahedral vacancies and amongst the three dopants Ge is the easiest to dope with.

CHAPTER 3

Doping Semiconductors

Introduction

Doping is defined as the introduction of impurities into an intrinsic semiconductor to modify the optical, electrical and structural properties of the material. The result of doping an intrinsic semiconductor with any trivalent or pentavalent material is an extrinsic semiconductor. The extrinsic semiconductor is of two types, p-type and n-type, and these materials are highly conductive in nature. In this chapter we outline the basic principles of semiconductor doping.

3.1 Basics principles of semiconductors

Semiconductors are materials that possess electrical properties somewhere in between those of conductors and insulators. Within a material, atoms can combine to form a solid (or liquid) by shifting or broadening their atomic energy levels to create energy bands. The valence band is the outermost energy level that contains the valence electrons. Semiconductors generally have a ‘half’ filled valence shell which implies that there are unoccupied energy states above the ‘half’ filled band that can be filled by an electron that is given the right amount of energy as shown in figure 3.1.

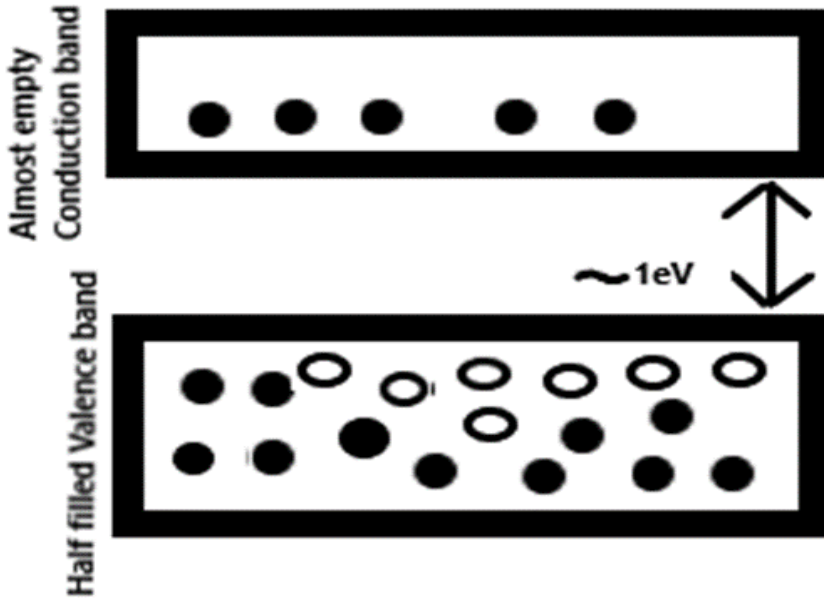

Figure 3.1. Schematic diagram illustrating an almost empty conduction and a half-filled valence band of a semiconductor [59].

Electrons that fill these unoccupied states are called free electrons, however, these free electrons are few because their atoms are closely packed in a crystalline pattern termed 'crystal lattice' (figure 3.2). When the valence band is completely filled the material is considered an insulator i.e. there are no unoccupied states in or above the filled valence band. An energy gap E_g called the forbidden energy band separates the valence band and the next available energy state that lies in the conduction band. There are no energy states that can be occupied by an electron within the forbidden energy band for a perfect material.

The electrical properties of a semiconductor can be enhanced by introducing donor or acceptor atoms within the material's crystal lattice. This action increases the amount of charge carriers within the material by producing more electrons than holes or vice versa. An n-type semiconductor contains impurity atoms that add electrons to the crystal lattice. The impurity atom creates a donor

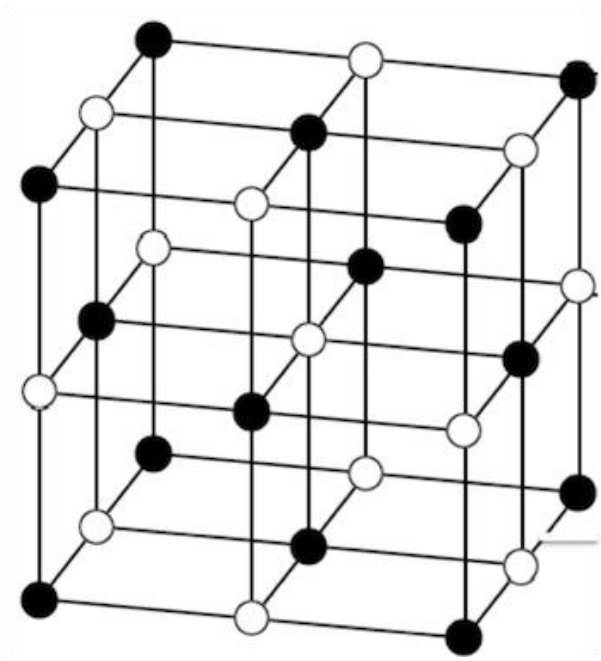

Figure 3.2. Schematic diagram of a basic crystal structure [60]

level inside the band gap of the material. The energy level of a shallow donor will be close to the lowest available energy level of the conduction band. To promote an electron from a donor level to an unoccupied state the probability is proportional to equation 3.1

$$e^{-E_D/kT} \tag{3.1}$$

where E_D is the energy level, k is Boltzman's constant and T is the temperature in Kelvin.

3.2 Carrier concentration and effect on band structure

The concentration of the dopant directly affects the concentration of the charge carriers within the material. In an extrinsic semiconductor under thermal equilibrium the number of holes p is equal to that of electrons n i.e.

$$n_i = p = n \tag{3.2}$$

and n_i is the materials intrinsic carrier concentration. Whereas for an extrinsic semiconductor under thermal equilibrium, for low doping, equation 3.2 becomes

$$n_i^2 = n_0 p_0 \tag{3.3}$$

where n_0 is the concentration of conducting electrons at thermal equilibrium and p_0 the hole concentration at equilibrium. The intrinsic carrier concentration is dependent on temperature and varies between materials [57,58].

Electron donor impurities create low energy states near the conduction band of a semiconductor while electron acceptor impurities create states near the valence band. The energy band gap that exists between these two bands is often referred to as the dopant-site bonding energy E_B and is relatively small. For instance, E_B for boron in silicon bulk is 0.045 eV as compared to silicon's band gap of about 1.12 eV. Therefore, since this energy is so small, thermal ionization can occur at room temperature and thus create free charge carriers in either band. Dopants also have the ability to shift the energy bands relative to the Fermi level as shown in figure 3.3. The energy band corresponding to the dopant with the highest concentration tends to shift towards the Fermi level. This leads to having a material with many useful electrical properties.

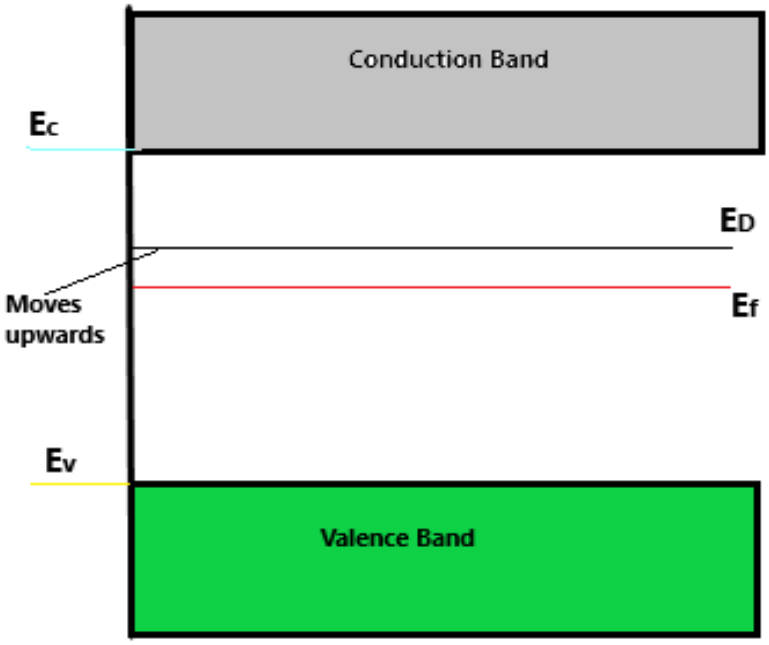

Figure 3.3. Schematic diagram illustrating energy band levels shifting relative to the Fermi level. Where E_C is the energy level of the conduction band, E_V the energy level of the valence band, E_f the Fermi level and E_D the energy level of the donor impurity [63].

3.3 Doping

Silicon is by far the most commonly used semiconductor material. A silicon atom contains four valence electrons in its outermost shell which it shares with its neighboring silicon atoms to form full orbitals of eight electrons (figure 3.4). The bonds in the pure silicon structure are stable because each atom shares one electron with its neighbor. This implies that there are very few free electrons available to move around the silicon crystal. However, by introducing an impurity atom such as phosphorus or antimony extra electrons are added to the lattice that allow current to flow easily. These atoms have five electrons in their valence shell to bond with neighboring atoms and are commonly known as pentavalent impurities.

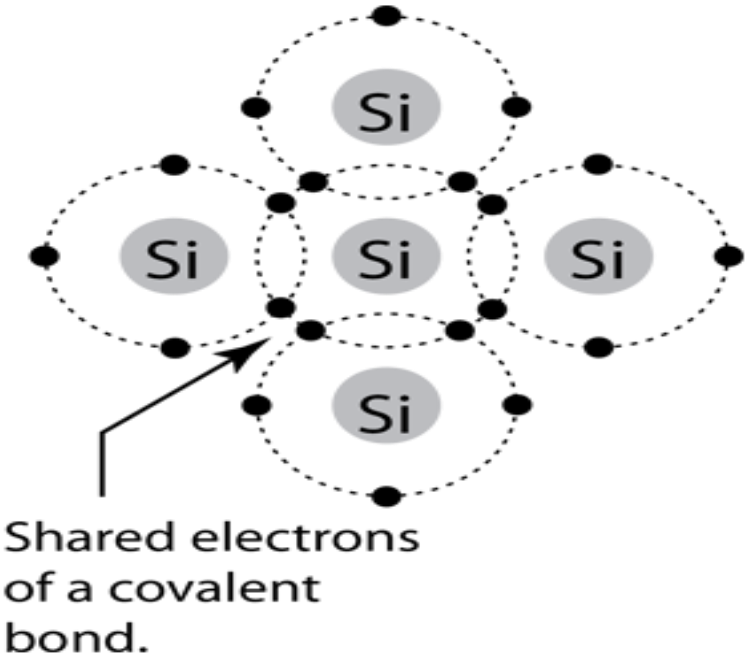

Figure 3.4. Schematic diagram of silicon covalent bonding [64].

A p-type semiconductor material on the other hand is one where an impurity atom removes an electron from the outermost orbital so that it can occupy a substitutional lattice site of the material. Elements such as indium and boron are trivalent, i.e. they have only three valence electrons in their outermost orbital. Thus, when they are introduced into the silicon lattice they have a hole and are able to attract a neighboring electron. However, the electron filling the hole leaves another hole behind it as it moves. This, in turn, attracts another electron, which, in turn creates another hole behind it, and so forth, giving the appearance that the holes are moving as a positive charge through the crystal structure (conventional current flow) illustrated in figure 3.5.

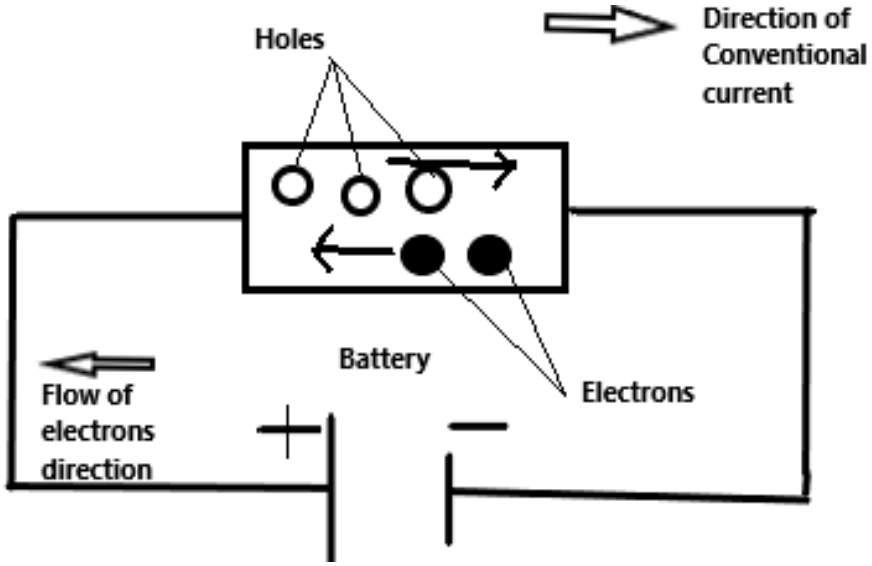

Figure 3.5. Schematic diagram of conventional current flow [65].

The impurity atoms are continuously generating holes by accepting electrons from the silicon atoms and thus are generally known as ‘acceptors’. The acceptor energy level is close to the valence band maximum and the probability that an electron will move from the valence band maximum to occupy an empty state in the acceptor level is proportional to equation 3.4

$$e^{-E_A/kT} \tag{3.4}$$

where E_A is the acceptor level, k the Boltzmann constant and T the temperature.

In an n-type semiconductor the majority carriers are electrons, while in a p-type material the majority carriers are holes. Extrinsic semiconductors are those whose conduction is increased by introducing dopant atoms. Generally, one can either use metal or non-metal elements to dope a material. Studies of elemental doping using non-metals are dominated by Si and P. For metal doping ion such as Ti^{4+} , Sn^{4+}, Zr^{4+} and Pt^{+} represent *n*-type dopants [60–68] while *p*-type dopants are represented by elements such as Mg^{2+}, Zn^{2+} , Ag^{+} and Cu^{2+} [69–77].

A study done by Chemelewski et al.[84] synthesized hematite (α-Fe_2O_3) porous thin films through coevaporation of pure Si and Fe in an oxygen ambient also known as reactive ballistic deposition. The aim of the study was to measure the photoelectrochemical water oxidation performance of the material under simulated solar irradiation. The results showed that the photoelectrochemical performance of Si-doped α-Fe_2O_3 improved compared to the undoped material. This is caused by improved photocurrents of porous films almost mainly due to increased charge transfer. Ultimately, the introduction of the Si dopant increased the water oxidation performance of porous hematite films.

Titanium ions (Ti^{4+}) have been investigated as a metal dopant as opposed to Si a non-metal dopant, among many other metal dopants, in hematite films and have proven to enhance the electrochemical properties of the material. Zhao et al. [85] prepared Ti-doped hematite nanorod thin films. These nanorods where characterized using scanning electron microscopy for thickness and morphology, X-ray diffraction to measure crystallinity, X-ray photoelectron spectroscopy for the chemical state of the material and a transmission electron microscope to analyze the selected area electron diffraction pattern and lattice structure. The results of this study showed that the doping of pristine hematite with Ti changes the morphology of the material. This is due to the fact that Ti in the solution promotes fast nucleation of hematite and

reduces the concentration of Fe^{3+} ions significantly. Furthermore, the photoelectrochemical performance of Ti-doped nanorod hematite films is enhanced compared to the undoped hematite. Ti increases the carrier density within the material and, as a result, the bulk charge separation and surface charge transfer are greatly enhanced and form active surface states.

One can further enhance the photocurrent density marginally through post-synthesis nitrogen treatment. Meng et al.[86] also showed from first principle calculations that modifying the energy band by doping α-Fe_2O_3 with a 3*d* transition metal ion such as Ti can improve the photoelectrochemical activity of the material. This was done using the density function theory (DFT)+*U* method. The results of the study showed that the band gap of hematite is ~2.1 eV and n-type dopant Ti improves the electric conductivity.

CHAPTER 4

Experimental methods

Introduction

Spectroscopy is the study of light and matter interactions. It is generally used as a tool to measure quantum energy levels in organic and inorganic molecules, atoms, semiconductors and many other materials. Molecules, for example, possess rotational and vibrational degrees of freedom and this motion is quantized. Hence, spectroscopy can be used to study and explain the spacing between these quantized states. This information can then be used to quantify bond strength and determine the whole molecular structure. This chapter gives a detailed explanation of the experimental procedures that were undertaken during this study. The processes of sample preparation and characterization are also outlined.

4.1 Raman Spectroscopy

4.1.1 Brief history

Raman spectroscopy was first introduced by C.V. Raman and K.F. Krishnan in the year 1928. C.V. Raman won the Nobel Prize in physics in 1930 for his discovery [87]. Raman spectroscopy was considered a nondestructive technique for chemical analysis in the 1930s. A great deal of challenges were encountered during this period with regards to a shortage of good light sources, very few good detectors, and inefficient filters to block the broad, fluorescence signal, which is several orders of magnitude stronger than the Raman signal.

The immergence of lasers in the 1960s led to a renewed interest in Raman spectroscopy and the development of the first Fourier transform Raman instrument in 1968 [88]. This instrument

enabled scientists to overcome the fluorescence problem. In 1990 the first dispersive Raman system was invented which included fiber optics, multichannel detectors and near-infrared lasers. During this period portable integrated dispersive Raman systems also emerged [89]. All this led to the extensive use of Raman systems in a variety of applications across multiple disciplines.

4.1.2 Raman spectroscopy

Raman spectroscopy is a nondestructive technique that relies on the scattering of electromagnetic radiation by molecules or atoms. It is a technique that provides detailed information about chemical structure, molecular interactions and crystallinity [90]. It investigates the rotational, vibrational and other low frequency modes of molecules such as external vibrations of a crystalline lattice obtained from the low-frequency regions of Raman spectra. This process happens through the scattering of photons by phonons when photons are incident on a material (figure 4.1). Raman spectroscopy often requires little to no sample preparation and can be performed directly through transparent holders such as cuvettes, glass containers, or plastic bags. Furthermore, it is a highly sensitive technique as it can differentiate molecules that are of similar nature but have slightly different vibrational properties.

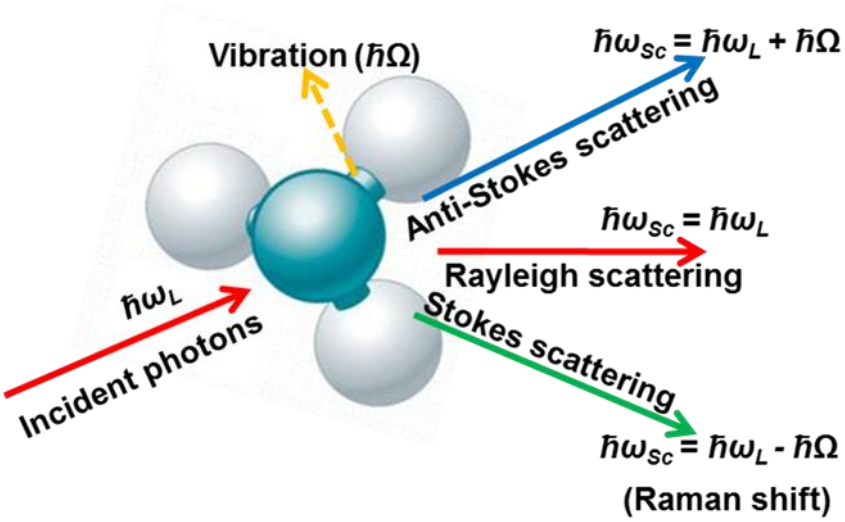

Figure 4.1. Schematic illustration of light scattering by Rayleigh, Stokes and Anti-Stokes scattering processes in a vibrating molecule due to the time-dependent perturbation introduced by incident photons. Here ω_L is the angular frequency of the monochromatic light source, Ω is the angular Raman frequency of the material and $\hbar$ is Plank's constant divided by 2π [91].

When photons are incident on a material, the interaction can be described by a time-dependent perturbation of the Hamiltonian. The perturbed system emits this photon and relaxes to its original state. Depending on the emitted photon frequency, this can lead to different scattering processes. These processes can be visualized by a quantum energy diagram shown in figure 4.2. The scattering processes that can occur are Rayleigh, Stokes and anti-Stokes scattering, the former being an elastic process, while the latter two are inelastic processes. In Stokes scattering the material absorbs energy and the emitted photon has a lower energy than the incident photon, whereas in anti-Stokes scattering the material loses energy and the emitted photon has a higher energy than the absorbed photon. Stokes scattering is the most probable process to occur compared to anti-stokes, and hence the Raman spectral measurements are Stokes measurement plots of the intensity of the scattered photon as a function of the difference between incident and scattered photon energy (i.e. Raman shift /or wavenumber) [92].

4.1.2.1 Stokes scattering

During Stokes scattering, an electron starts in the ground vibrational state of the ground electronic state, is promoted to a virtual state and then relaxes to a vibrational energy level that is higher than the initial vibrational level. In anti-Stokes scattering, the electron transitions from a vibrational state that is higher in energy than the ground state to a virtual state and then relaxes back to the ground vibrational state. Raman scattering is generally an inefficient process: typically only 1 in 10 million incident photons are Raman-scattered [93].

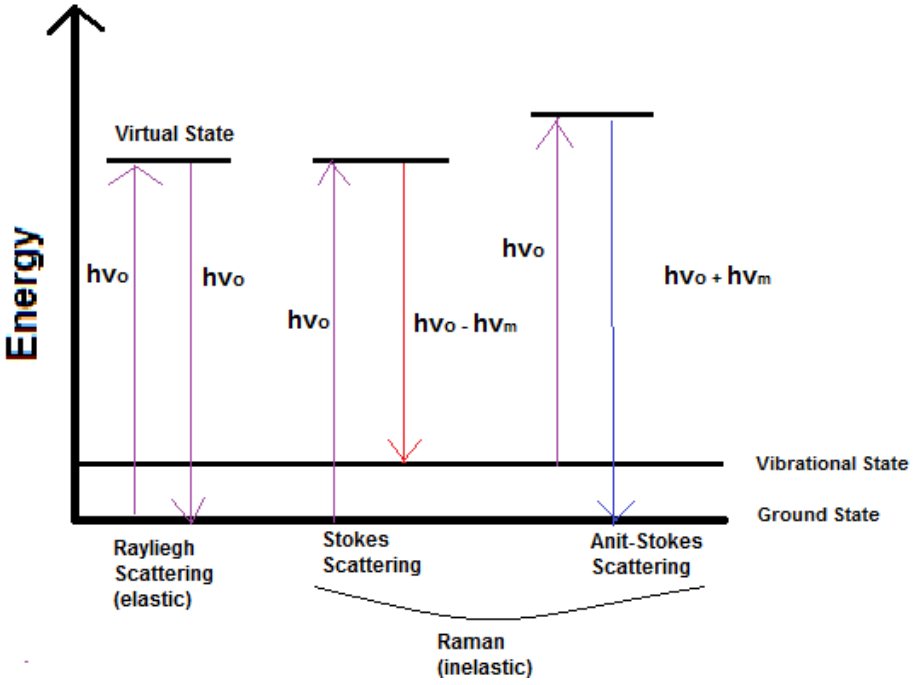

Figure 4.2. Raman scattering illustrated in a quantum energy diagram where h is Plank's constant and v_0 and v_m are the frequencies of the electric field and the molecular vibrations, respectively.

4.1.2.2 Typical Raman spectroscopy experimental setup

A schematic diagram of a typical Raman spectroscopy experimental setup is shown in figure 4.3. A laser is used as an excitation source which provides monochromatic light to excite the molecules. The light travels from the light source to the beam expander and the Rayleigh filter, which is a dichroic beam splitter that acts as a short-pass filter. It is then reflected off a mirror

into a microscope where it is directed onto the sample. The scattered light is collected and then directed by a focusing mirror onto a grating where it is dispersed. The dispersed light is then focused into a detector [94].

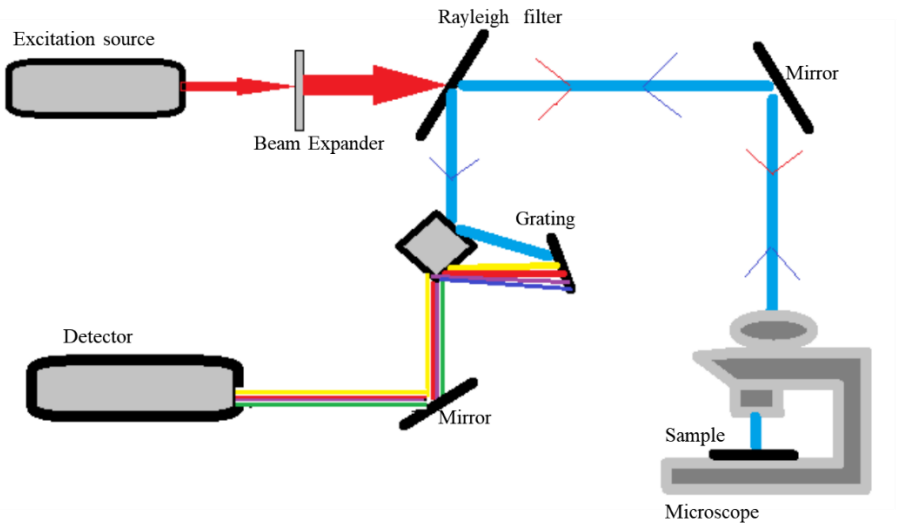

Figure 4.3. Schematic illustration of a typical Raman spectrometer instrument.

4.1.3 Confocal Raman microscopy with an integrated AFM unit.

Confocal Raman microscopy is based on point-to-point image formation. Figure 4.4 illustrates this technique, where light from a point-like source (laser) is reflected by a dichroic filter that reflects wavelengths longer than the specified wavelength called the cut-off wavelength, a built-in property of the filter, and transmits shorter wavelengths. The light is then focused to a diffraction limited spot in the focal plane by an objective lens. The focal spot size on the sample is dependent on the wavelength and the quality of the beam and the radius is given by:

$$r \approx 0.61 \frac{\lambda}{NA}$$

where λ denotes the wavelength of the light, NA ($=n \sin \theta$) the numerical aperture which is defined by the product of the refractive index of the medium and the sine of the semi-aperture

angle. The image spot is then reflected form the focal plane back through the objective and directed towards the dichroic filter. The filter is designed such that a fraction of the excitation beam will be directed towards the sample from the focal plane and the rest of it will be transmitted i.e. when the light is scattered, the filter transmits longer wavelengths, stokes scattering, and blocks Rayleigh scattering. The light is then focused onto a pinhole. The aperture size is carefully chosen so that only the central part of the focus is let through to reach the detector. The pinhole acts as a second 'focal plane', or a confocal plane. Light rays that do not emanate from the focal plane will not be let through the aperture. Therefore, confocal Raman microscopy allows for two main advantages over conventional microscopy: by scanning a sample with respect to the objective one can form a high resolution 3D image. Secondly, the contrast of an image is greatly enhanced because only light from the focal plane will reach the detector. Furthermore, one can get a $\sqrt{2}$ improvement of the image quality for an infinitely small pinhole. Thus, for a suitable aperture diameter there is a trade-off between the intensity and resolution [95]. This allows one to obtain the depth information of a sample.

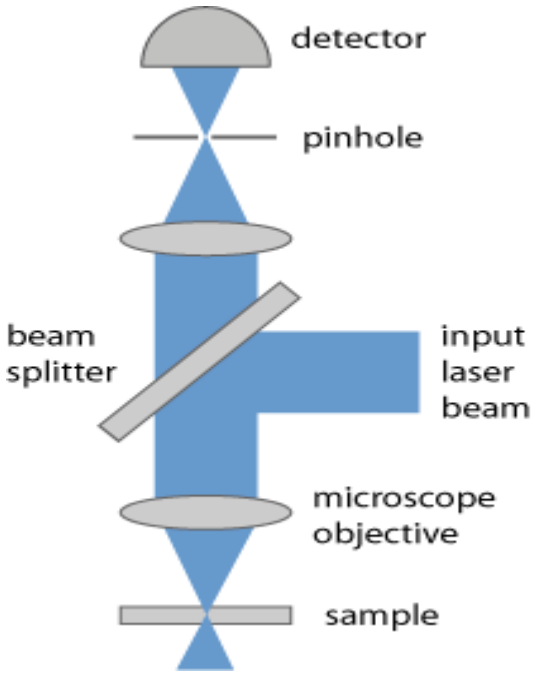

Figure 4.4. An illustration of the confocal microscopy principle. The yellow incoming beam indicates the laser source used to excite the sample. The dichroic beam splitter transmits wavelengths longer than the cut-off wavelength, a built-in property of the filter, and reflects shorter wavelengths. The light is focused to a diffraction limited spot in the focal plane by an objective lens. The red lines indicate the image spot from the sample in the focal plane. The dotted lines indicate the path the light would follow if it were directed from before or after the focal plane. The light from the focal plane (red lines) is then directed through the objective to the dichroic filter. If the wavelength of the light is longer than the cut-off wavelength of the dichroic filter it is transmitted to the second focal plane (pinhole). Only light rays emanating from the first focal plane will be let through [96].

Atomic Force Microscopy (AFM) is a high-resolution imaging technique used to study surface roughness (topography and morphology) and the particle size of samples. AFM operates either on contact or non-contact (i.e. tapping) mode by measuring the force between a cantilever tip and the sample surface. In AFM imaging (contact mode), a force between the sample surface (in contact with the tip) and the cantilever tip bends the cantilever when the tip encounters features on the sample surface. This deflection is sensed and reflected by a laser beam onto a segmented photodiode from which the AFM topographic map of the sample surface is obtained (Figure 4.5). In non-contact mode, the sample surface is in intermittent contact with the cantilever tip (the tip oscillates over the sample); however, the deflection of the cantilever is still sensed and reflected as in contact mode to produce a height image. For this work the non-contact mode was used.

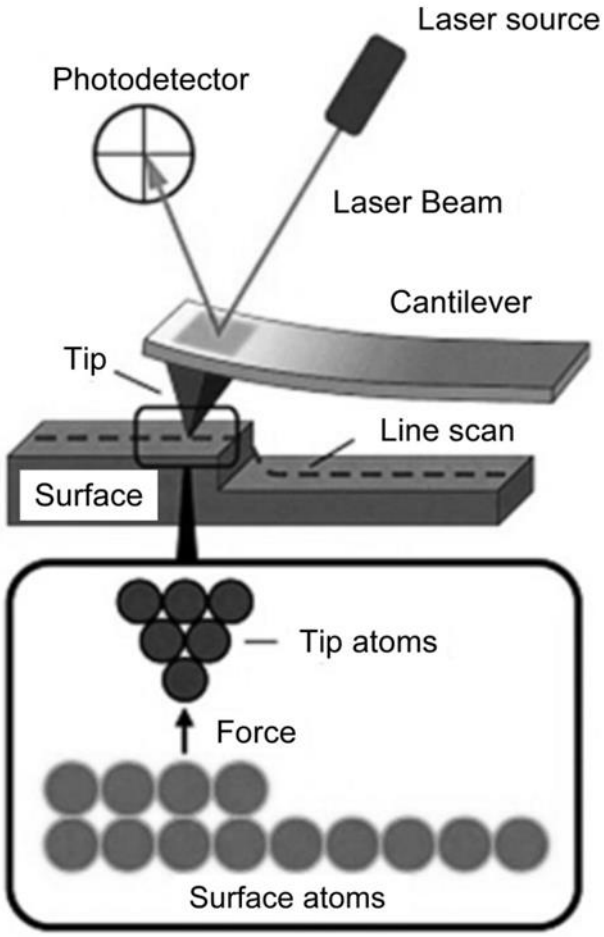

Figure 4.5. Schematic diagram of an AFM. It operates either in contact or non-contact (or tapping) mode by measuring the force between a cantilever tip and the sample surface to produce a topographic image [97].

4.2 Ultrafast Transient Absorption Spectroscopy

Ultrafast spectroscopy is a technique that requires temporally short laser pulses to investigate the transient dynamics of an electronically or vibrationally excited system rather than the energy levels themselves. Ultrafast transient absorption spectroscopy allows us to look at the absorption properties of molecules that exist in the ground state or excited state. Since the excited states are generally short-lived, at times-scales such as picoseconds (ps), this technique makes use of laser pulses with a duration in the order of femtoseconds, i.e. sub-ps. This is

important because the duration of the laser pulses must be shorter than the time scale of the dynamics that one wants to observe.

4.2.1 Femtosecond laser

The femtosecond laser plays a pivotal role in a femtosecond transient absorption spectroscopy setup. The laser is designed to emit optical pulses, with a duration well below 1 ps, called ultrashort pulses in the domain of femtoseconds (fs). These pulses are almost always achieved through a technique called passive mode locking. This technique involves incorporating light absorbers with a degree of absorption which is reduced at high optical intensities into the laser cavity. There a several types of femtosecond lasers that can be found in the market for different purposes depending on one's experimental needs. Passively mode-locked solid-state bulk lasers can produce high-quality ultrashort pulses with pulse durations between 30 fs and 30 ps and typical average output powers between ~ 100 mW and 1 W. Titanium–sapphire lasers can emit pulses below 10fs to approximately 5 fs. The pulse repetition rates typically range between 50 and 500 MHz. There are also low repetition rate lasers with a few kilohertz for higher pulse energies and smaller lasers with repetition rates of tens of gigahertz. There are a few important aspects to take into consideration with regards to femtosecond lasers which are the following:

- Pulse duration - defined as the duration of an optical pulse. In practice the pulse duration is most frequently obtained from full width at half-maximum (FWHM) of the optical power versus time. Pulse durations reaching ~10 ps can easily be measured with autocorrelation or cross-correlation techniques. There are also techniques such as frequency-resolved optical gating (FROG) and spectral interferometry (SPIDER) that are used for the full characterization of ultrashort pulses, i.e. measuring full time-dependent electric field along with the pulse parameters such as the pulse energy or pulse duration.
- Pulse repetition rate - defined as the number of pulses emitted per second.

- Average output power and pulse energy- by taking the integral of the optical power over time one will obtain the pulse energy.
- Noise properties - These can differ depending on the model and types of the femtosecond laser. Noise includes timing jitter, intensity noise and various types of phase noise.

4.2.2 The pump-probe method

In order to understand the basics of light-induced processes it is necessary to study the elementary steps with time-resolved techniques on a molecular level. The most prominent method to study these processes is transient absorption spectroscopy. Figure 4.6 illustrates the experimental approach which is the use of pump-probe spectroscopy, a two-pulse technique that allows one to investigate photophysical and photochemical processes on any time scale. This technique makes use of two ultrashort pulses, known as the 'pump' and 'probe' pulses to excite a sample. The pump pulse arrives first which perturbs the sample to vary the population in the ground state or excite a sub-population to an electronically excited state. It is followed by a subsequent probe pulse that arrives at the sample at a specified delay time Δt and its absorption spectrum is measured. The probe pulse is then dispersed into individual wavelength components after interaction with the excited sample, using a dispersive grating, and recorded by an array of ultra-sensitive pixels. In the pump-probe technique the time resolution is dependent on a few factors: the duration of the pump and probe pulses, the extent to which the delay time between them is controlled and their relative temporal jitter [98]. The measurement can be repeated over a long period of time by increasing the delay time between the pump and probe pulses. The measurements can be tracked from a point of reference known as time zero ($\Delta t=0$), where both probe and pump pulses overlap temporally, i.e. arrive at the sample at the same time. The delay time is given by

$$\Delta t = \frac{d - d_0}{c}$$

where d denotes the distance travelled by the delay line relative to d_0 which denotes the position where both pulses overlap temporally at the sample. The speed of light in a vacuum is represented by c in the equation.

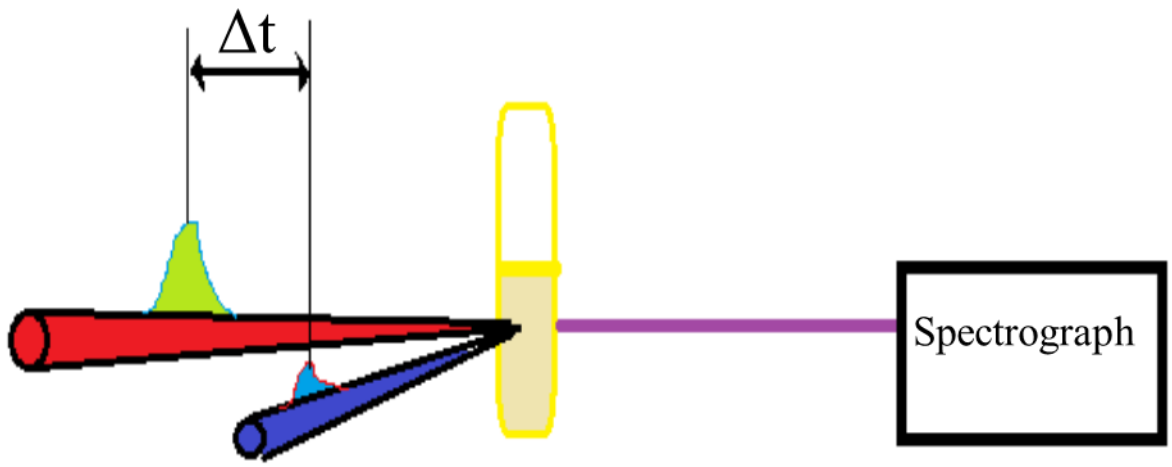

Figure 4.6. Schematic representation of a pump-probe experiment. The larger cross-sectional area of the pump pulse than that of the probe ensures that only the pumped section of the sample is probed.

4.2.3 Signal detection (Beer–Lambert law)

The amount of light a material absorbs can be directly correlated to the concentrations of attenuating molecules within the material as well as the thickness of the sample. The relationship between these parameters is known as the Beer–Lambert law. When monochromatic light passes through an absorbing medium, a transparent hematite coated glass substrate for instance, there is an exponential decrease in the intensity of the transmitted light.

This is because when light enters the sample it interacts with the molecules and can be absorbed, transmitted or scattered [99]. Hence the Beer-Lambert law is given as follows:

$$I = I_0 e^{-\varepsilon l \mathrm{C}} \tag{4.1}$$

where I is the pump beam intensity after passing through the sample, I_0 the intensity before the sample, ε the molar extinction coefficient of the material, l the path length of the sample and C the concentration of the sample. When conducting a pump-probe experiment we are interested in the absorbance A, or the optical density $OD\ (= \varepsilon l C)$ which can be obtained by taking the logarithm of equation (4.1):

$$OD(\lambda, \Delta t) = log \frac{I_0(\lambda)}{I(\lambda, \Delta t)} \tag{4.2}$$

Ultrafast TA spectroscopy measures the time-dependenct absorption of a sample after excitation. Thus, an absorption measurement which measures the probe pulse, can be made on the system in the unexcited state, denoted by $A_{pumpOFF}(\lambda, \Delta t)$, subtracted by an absorption measurement of the system in the excited state, $A_{pumpON}(\lambda, \Delta t)$, to obtain an absorption signal that gives information about the absorption changes related to the molecules within the sample. One can generate an absorption spectrum with OD values at different wavelengths of the pumped sample by varying the delay times between the pump and probe pulses. Sequential pump-on and pump-off measurements are performed using an optical chopper that blocks every second pump pulse [100]. The quantity ΔOD is given by the equation:

$$\Delta OD\ (\lambda, \Delta t) = A_{pumpON}(\lambda, \Delta t) - A_{pumpOFF}(\lambda, \Delta t) \tag{4.3}$$

Thus, from the Beer-Lambert law and equation (4.2) ΔOD becomes:

$$\Delta OD = -\log\left(\frac{I_{ON}}{I_{OFF}}\right) \tag{4.4}$$

where I_{ON} denotes the transmission intensity of the excited states of the sample (pump-on) and I_{OFF} that of the unexcited states of the sample (pump-off). In the case where a third beam is used, known as the reference pulse which is identical to the probe pulse, that passes through the sample at an unexcited spot to assist in suppressing noise [101], equation (4.4) becomes:

$$\Delta OD = -\log\left(\frac{I_{ON}}{I_{OFF}}\right)$$

$$= -log\frac{(I_{\lambda,\Delta t}^{Probe})/(I_{\lambda,\Delta t}^{Ref})}{(I_{\lambda}^{Probe})/(I_{\lambda}^{Ref})} \tag{4.5}$$

where $I_{ON} = (I_{\lambda,\Delta t}^{Probe})/(I_{\lambda,\Delta t}^{Ref})$ is the ratio of the probe and reference beam intensities at a specific pump excitation wavelength and delay time after the sample has been excited. $I_{OFF} = (I_{\lambda}^{Probe})/(I_{\lambda}^{Ref})$ is the ratio for when the sample has not been excited [66][67]. Change in absorption (ΔA) measurements are taken between pump on and pump off delay times and are plotted as a function of wavelength.

The pump-probe signal is the sum of three main contributors which are the ground state bleach (GSB), stimulated emission (SE) and excited state absorption (ESA). In the context of semiconductors, ESA can be divided into excited electron absorption and hole absorption.

During GSB at the wavelength of the pump pulse, the population of electrons in the ground state are depleted and hence reducing the absorption capabilities of the material, thus giving rise to a negative ΔA signal. SE occurs when an excited electron interacts with a photon of the probe pulse which then results in the emission of two photons. SE makes an overall negative contribution to ΔA signal due to the increased emission causing a decrease in the A_{pumpON} absorption spectrum. ESA occurs when an excited electron interacts with the probe pulse and transitions to a higher electronic state. This is due to the photons being absorbed by the lower energy electrons, which then results in the signal of the ΔA spectrum being positive.

4.2.4 Data Analysis

Ultrafast TA pump-probe spectroscopy experiments are complex, in the sense that the raw data collected is a three-dimensional dataset consisting of absorption difference intensities as a function of the wavelength λ and delay time Δt. These datasets can typically have up to thousands of distinct data points for each measured spectrum. Thus, extracting useful information from this type of data can be a daunting task. One can attempt to deconvolute the data by selecting a kinetic trace at a particular wavelength or a line spectrum at a certain delay time. However, this does not adequately represent the system as a whole. Global analysis and target analysis are sophisticated methods for time-resolved data analysis [103]. These methods can be successfully conducted using Glotaran [104], an advanced, open-source software for data analysis. Global and target analysis models assume that the data collected is homogeneous and therefore it can be described by a single, discrete set of separable parameters. The data can be described by a data matrix Ψ which is a superposition of the contributions of the n_{comp} different components given by the equation:

$$\Psi(\lambda, t) = \sum_{l=1}^{n_{comp}} c_l(t)\varepsilon_l(\lambda) \tag{4.6}$$

where $c_l(t)$ is the concentration or fractional amplitude of the l^{th} component and $\varepsilon_l(\lambda)$ is the spectrum of the l^{th} component. Generally, to get an idea of the kinetic scheme in global analysis one initially performs singular vector decomposition (SVD), which helps determine the number of independent components within the raw data. The SVDs with a well-defined structure (distinct from noise signals) will help determine the number of initial components to be used for data fitting. This number can vary depending on the sample. To measure the quality of the fit one can look at the convergence of the sum of square errors with increasing iterations. Furthermore, for a good fit the residuals should be structureless. For global analysis in Glotaran, one can run a sequential kinetic scheme on the raw data which yields evolution associated difference spectra (EADS) or a parallel kinetic scheme which yields decay associated difference spectra (DADS). EADS are governed by a model that consists of independent compartments that sequentially decay into one another. Target analysis yields species associated difference spectra (SADS). Using equation (4.6) we can again mathematically describe the model that produces EADS as follows:

$$\Psi(\lambda, t) = \sum_{l=1}^{n_{comp}} c_l^{EADS}(t, \theta) EADS_l(\lambda) \tag{4.7}$$

EADS result in mixed states, as opposed to one pure state, primarily because one decays into another with successive lifetimes. Therefore, if one needs to isolate a system for analysis, target analysis can be employed which is a compartmental model and can be described by the following equation:

$$\Psi(\lambda, t) = \sum_{l=1}^{n_{comp}} c_l^{SADS}(t, \theta) SADS_l(\lambda) \quad (4.8)$$

DADS can be computed from SADS or EADS because the DADS model is mathematically equivalent to either of the models.

4.3 Sample preparation

The transparent hematite thin films were prepared on the fluorine-doped tin oxide coated glass substrates by spraying a metal salt solution of Fe_2O_3 onto a heated substrate (Figure 4.7). The setup entails a substrate heater, spray gun, air compressor, solution reservoir and a gas exhaust gas unit [105].

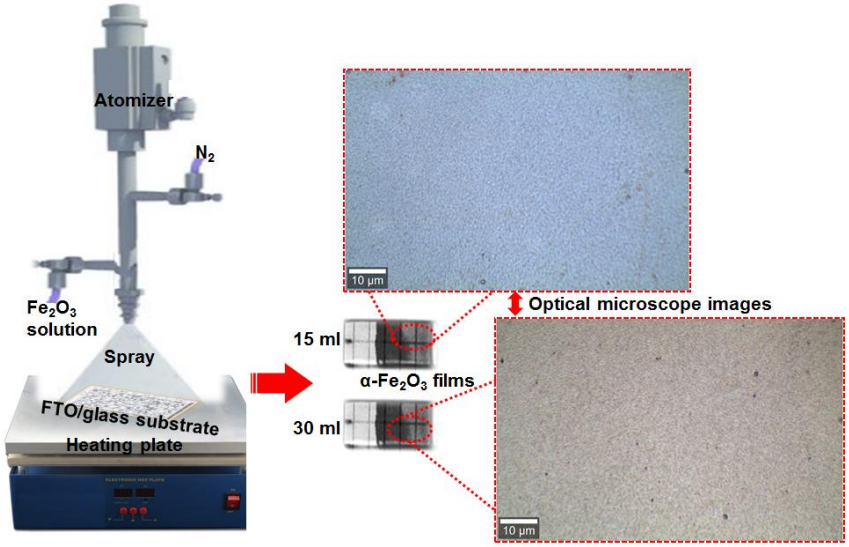

Figure 4.7. Schematic diagram of the basic components of spray pyrolysis setup.

In figure 4.7, the optical microscope images show the different hematite samples prepared by spray pyrolysis with Fe_2O_3 volumes of 15 ml and 30 ml. It is worth mentioning that the Fe_2O_3 spray volumes in the range ~10 – 30 ml exhibit continuous thin films with a negligible agglomeration of nanoparticles. From each volume set of hematite samples, one sample was

treated with tetraethoxysilicate (TEOS) without post-annealing (samples 2) and another sample was post-annealed at 500 ºC for 2 h with 10 ºC/min ramping without TEOS treatment (samples 3). The fourth samples from each volume set were both treated with TEOS and post-annealed to be compared to the untreated sample 1.

Table 1. Different hematite films prepared using 15 and 30 ml of the spray pyrolysis solution; and post-treated or untreated and annealed. Where "Yes" means the treatment has been applied to the sample.

Treatment	**15 ml**				**30 ml**			
	Sample 1	Sample 2	Sample 3	Sample 4	Sample 1	Sample 2	Sample 3	Sample 4
TEOS	No	Yes	No	Yes	No	Yes	No	Yes
Post-annealing @ 500 °C	No	No	Yes	Yes	No	No	Yes	Yes

4.4 Characterization

4.4.1 Confocal Raman microscopy

WITec alpha300 RAS+ confocal Raman microscope (high-resolution confocal Raman imaging with integrated atomic force microscopy (AFM)) was used for analysis/imaging of the thin films. Acquisition of image scans and/or spectroscopy data was carried out using a 532 nm excitation laser (laser power of 5 mW) and ×100 Zeiss objective which gives a diffraction limited lateral and depth resolution of about 360 and 530 nm, respectively. The surface image scans were acquired over 40 × 40 μm^2 area and the depth profiles over a depth of 20 μm and a width of 30 μm with 100 points per line and 100 lines per image using an integration time of 3

s. For AFM imaging (AC mode), a ×20 Zeiss objective was used fitted with the cantilever with a spring constant of 2.8 N/m and a nominal resonance frequency of 75 kHz.

4.4.2 Transient absorption spectroscopy

Transient absorption (TA) spectroscopy measurements were performed using a Clark-MXR, Ti: Sapphire femtosecond laser source, which operates at a 1 kHz repetition rate with a pulse duration of 150 fs centered at 775 nm. A 70:30 beam splitter was used to split the fundamental laser beam into a pump and probe beam, with an average output power of 249 mW and 581 mW, respectively. The pump beam was sent through a beta barium borate (BBO) crystal for frequency doubling, producing a beam centered at 387.5 nm. The pump fluence at the sample was 1.02mJ.cm^{-2}. A chopper was placed in the path of the pump beam to block every second pulse so that the frequency was halved to (500Hz), thus generating sequential pump-on and pump-off measurements. The probe beam was passed through a 2 ns delay line before being focused into a 4 mm sapphire crystal to produce a broad white light continuum in the wavelength range of 430 to 680 nm. The probe and pump beams were directed into the sample where they overlapped temporally and spatially. After the sample, the pump beam was blocked and the probe pulses were carefully aligned into a fiber cable connected to a spectrograph which dispersed the probe onto a CMOS sensor + PD digitiser (Glaz LineScan-I) so that the transmitted intensity could be recorded. Measurements were performed using a custom-written MATLAB interface. Pump-probe measurements give difference absorption ($\Delta A = A_{\text{pumped}} - A_{\text{unpumped}}$) spectra. Glotaran software [106] was used to analyze the obtained data to find the evolution associated difference spectra and associated decay lifetimes.

CHAPTER 5

Results and discussion

Introduction

In this chapter we present the results and discussion of the confocal Raman microscopy and pump-probe transient absorption spectroscopy measurements. We discuss the Raman characteristic features of hematite, depth profiles, surface roughness as well as AFM measures. Furthermore, pristine hematite was prepared under 3 experimental parameters and we present the decay lifetimes under each experimental parameter and their implications.

5.1 Confocal Raman microscopy

Amongst other characterization techniques, Raman spectroscopy is a preferred method for hematite analysis since it is non-destructive and provides information on crystallinity, composition and phase identification of different structures and the effect of disorder in the films. Hematite has a corundum structure, and for this structure, group theory proposes seven first-order Raman-active vibrational modes, i.e. two A_{1g} and five E_g symmetries at the center of the Brillouin zone. Briefly, hematite has seven characteristic spectral features which are vibrational modes at 229, 247, 297, 302, 414, 500 and 615 cm^{-1} (see figure 5.1(a) and 5.1(b)). The vibrational modes at 229 and 500 cm^{-1} are assigned to A_{1g} symmetry while the other five modes (247, 297, 302, 414 and 615 cm^{-1}) are assigned to E_g symmetry. It can be seen from figure 5.1(a) and 5.1(b) that the as-prepared thin films exhibit the Raman characteristic spectral features of hematite material, as expected. In figure 5.1(c), it can be seen that the Raman spectra of the films prepared using both 15 and 30 ml of the spray pyrolysis solution do not show peak-

shifting suggesting that the films have a similar average particle size [34], [107]–[110]. The films prepared using 30 ml of the spray pyrolysis solution display higher intensity peaks at 229 and 297 cm^{-1} compared to 15 ml samples (Figure 5.1(c)), suggesting that the 30 ml samples are slightly thicker than the 15 ml samples. Certainly, the intensity of the Raman scattering is proportional to the density of the interacting media.

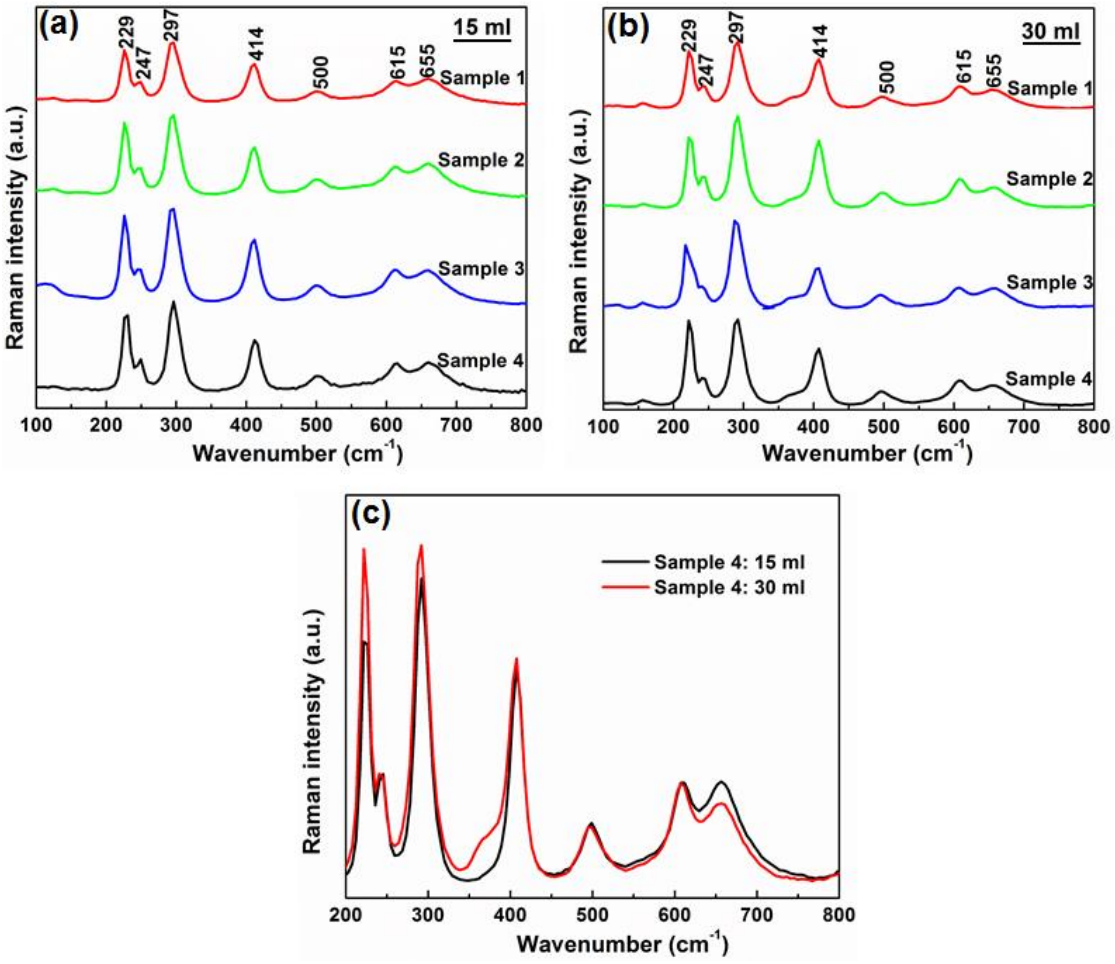

Figure 5.1. Raman spectra of different hematite samples prepared by spray pyrolysis with a volume of (a) 15 ml and (b) 30 ml, for each spray volume Sample 2 was post-treated, Sample 3 annealed and Sample 4 the combination of TEOS treatment and annealing. (c) Raman spectra of Sample 4 for both 15 and 30 ml spray volume.

To investigate the uniformity of the film on the FTO substrate, a Raman intensity map of the 297 cm^{-1} peak was obtained for each sample. Figure 5.2 shows the optical microscope images with an overlain Raman mapping for all the as-prepared samples. The uniform intensity of the mapping suggests a uniform composition (phase) of hematite across the analyzed areas of the samples. This suggests that a uniform coating of the hematite film was achieved on the substrates. In addition, the reduced surface roughness of the films seen from the optical microscope images confirms the uniform and conformal coverage across the FTO substrates.

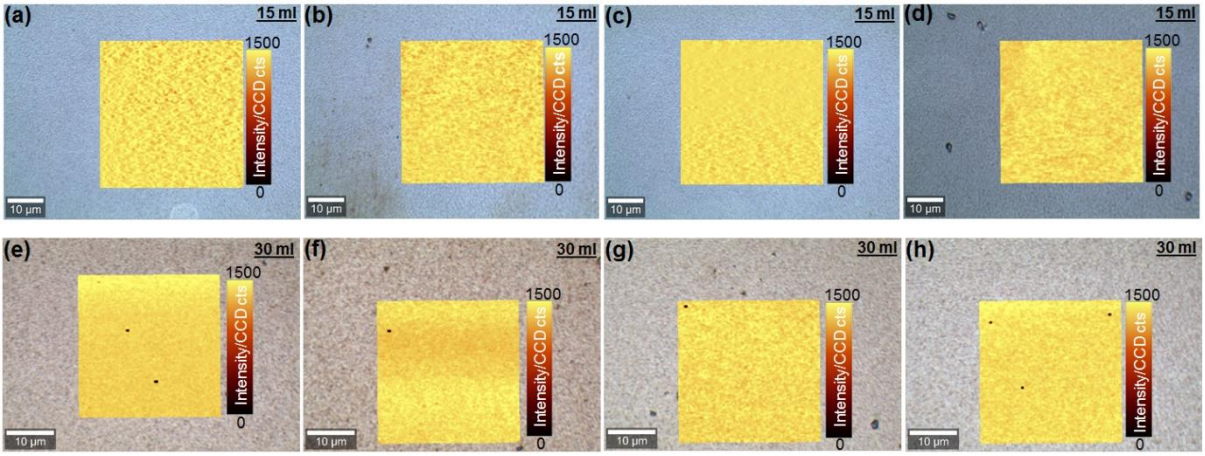

Figure 5.2. Optical microscope images with an overlain Raman intensity mapping of the 297 cm^{-1} peak of different hematite samples prepared by spray pyrolysis with a volume of (a-d) 15 ml and (e-h) 30 ml, and post-treated or untreated and annealed.

Moreover, the confocal Raman microscopy depth profiles were used to obtain the thickness of the prepared films by mapping the intensity of the 297 cm^{-1} peak of as-prepared hematite samples (see figure 5.3(a-h)). From the depth profiles, it can be seen that air and FTO/glass exhibit no signal with a phonon band at 297 cm^{-1}. Average depth line profiles were obtained (see figure 5.3(i and j)) and fitted with a Lorentzian function. The FWHM of the fitted curves represent the thickness of each as-prepared hematite film, as shown in figure 5.3(k). The FWHM method (or 50% maximum intensity method) is used with the assumption that the

actual interface appears at 50% of the maximum Raman intensity and the diffraction limited depth resolution at each interface is at best about 530 nm. From the thicknesses of the as-prepared hematite films for both 15 and 30 ml of the spray pyrolysis solution, it can be seen that the unannealed films (TEOS treated and untreated) display comparable thicknesses in the order of 800 nm. On the other hand, annealed films display thicknesses in the order of 600 nm. However, the films prepared using 30 ml of the spray pyrolysis solution show slightly thicker layers compared to the 15 ml solution.

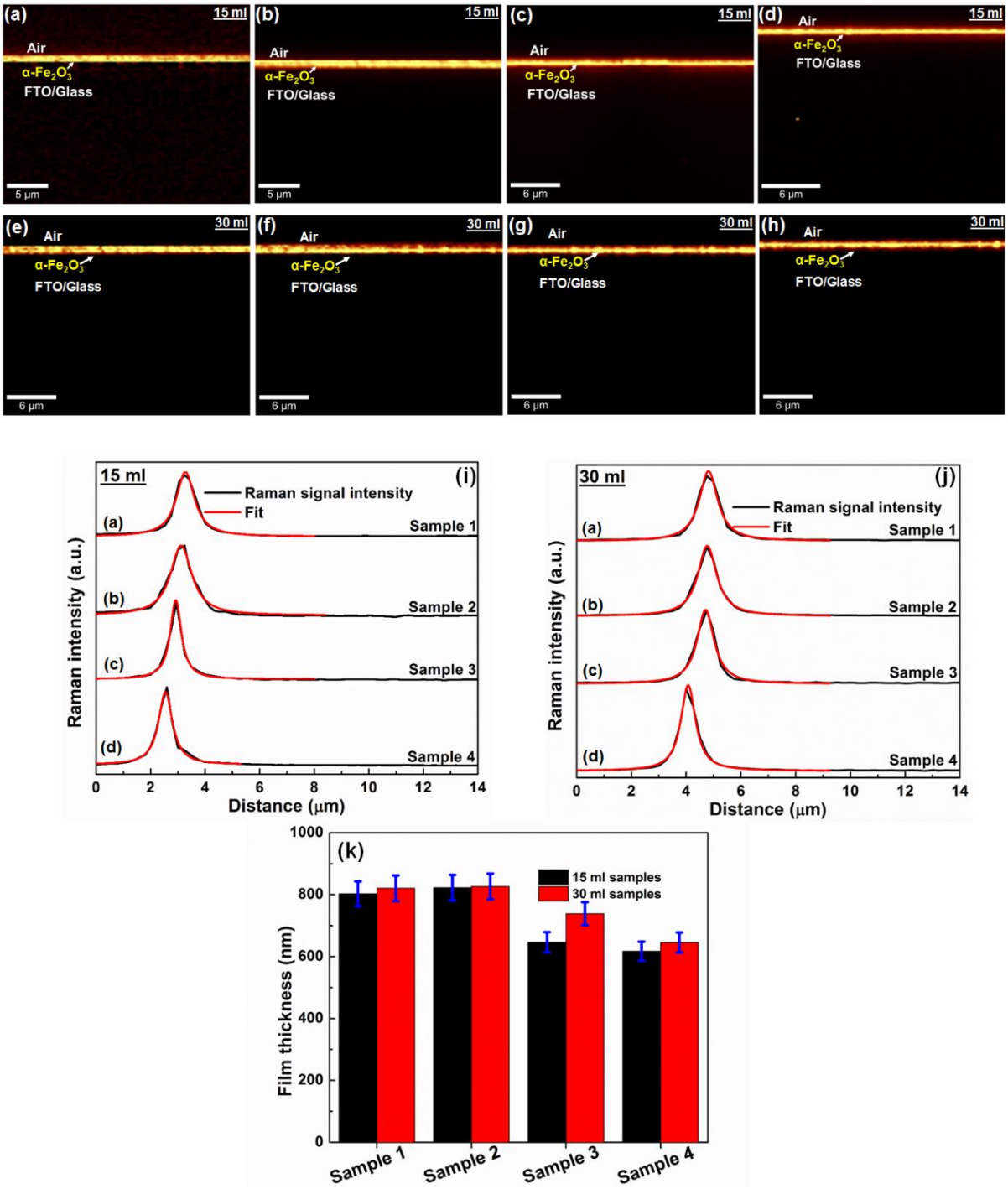

Figure 5.3. Raman depth profiles (cross-section image) obtained by mapping the intensity of the 297 cm^{-1} peak of different hematite samples prepared by spray pyrolysis with a volume of (a-d) 15 ml and (e-h) 30 ml, where samples were post-treated, annealed and a combination of these two. (i and j) Average depth line profiles (black) corresponding with (a) to (h) and fitted with a Lorentzian function (red). (k) Thickness of the as-prepared hematite films for each of the samples for 15 ml (black)) and 30 ml (red) of the spray pyrolysis solution.

The surface roughness of the films was investigated using atomic force microscopy (AFM) and the results are presented in figure 5.4(a-h). The average surface roughness values obtained from the AFM images of the films are plotted in figure 5.4(i). The hematite films prepared using 15 ml of the spray pyrolysis solution display average surface roughness values (~6 nm) smaller than those prepared using 30 ml (~9 to 10 nm). Nonetheless, the reduced surface roughness (<10 nm) of the films further confirms the observed reduced roughness of the films from the optical microscope images which in turn confirms the uniform and conformal films coverage across the substrates. Moreover, the average particle size of the films was estimated from the AFM images (Figure 5.4(a-h)), as shown in figure 5.4(j). The unannealed films (TEOS treated and untreated) display a slightly larger average particle size (17.5 – 19.5 nm) compared to the annealed films (16.8 nm). In general, the as-prepared films for both 15 and 30 ml of the spray pyrolysis solution display a comparable average particle size. Though we do not observe an obvious difference in the average particle size for both 15 and 30 ml of the spray pyrolysis solution, it is expected that the size would increase with an increase in the amount of Fe_2O_3 precursor because the reactant with the higher amount enhances the merging of crystal nuclei and agglomeration of particles.

Briefly, the thickness and the surface roughness and the particle szie of the thin films changed significantly under treatment of TEOS and annealing. Treatment of both annealing and TEOS ultimately resulted in thinner and much smoother films; however, the average particle size was comparable for both treatments (see Table 2).

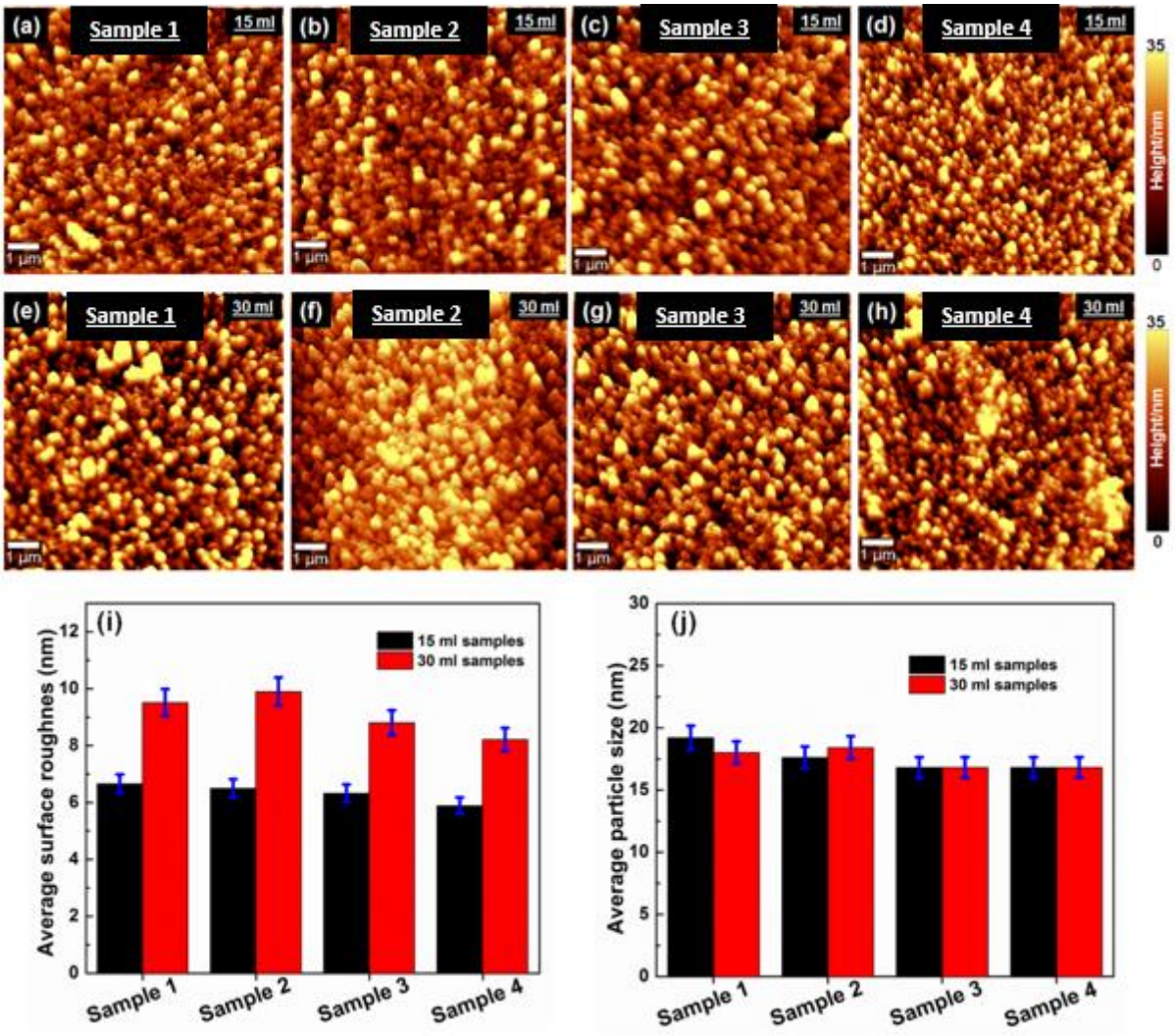

Figure 5.4. (a-d) AFM surface images of different hematite samples prepared by spray pyrolysis with a volume of (a-d) 15 ml and (e-h) 30 ml, and post-treated (Sample2) or untreated and annealed (Sample3). (i) Average surface roughness, corresponding to (a)- (h). (j) Average particle size, corresponding to (a)-(h).

Table 2. The thicknesses, average surface roughness and particle size of different hematite films prepared using 15 and 30 ml of the spray pyrolysis solution; and post-treated (Sample 2), annealed (Sample 3) and a combination of these two (Sample 4).

Treatment	15 ml				30 ml			
	Sample 1	Sample 2	Sample 3	Sample 4	Sample 1	Sample 2	Sample 3	Sample 4
TEOS	No	Yes	No	Yes	No	Yes	No	Yes
Post-annealing @ 500 °C	No	No	Yes	Yes	No	No	Yes	Yes
Film thickness (nm)	802	822	646	617	820	826	738	645
Film roughness (nm)	6.7	6.5	6.3	5.9	9.5	9.9	8.8	8.2
Film particle size (nm)	19.2	17.6	16.8	16.8	18.0	18.4	16.8	16.8

5.2 Transient absorption spectroscopy

A 2-dimensional transient absorption (TA) intensity map of pristine hematite films (i.e. Sample 1 in table 1 for 15 ml spray volume) is shown in figure 5.5. The measured TA signal is a sum of at least three contributions, namely, excited state absorption (ESA) of electrons and holes, ground state bleach (GSB) and stimulated emission (SE). On the map, two time scales can be distinguished: fast decay of the broadband ESA signal within the first few ps, followed by a much slower decay of this signal within several tens of ps. The main spectroscopic feature of this map is the ESA signal that peaks around 570 nm which is ascribed to absorption of mainly photo-generated holes [111]. All 8 samples have similar spectroscopic features which agree with earlier studies on hematite thin films [27][112].

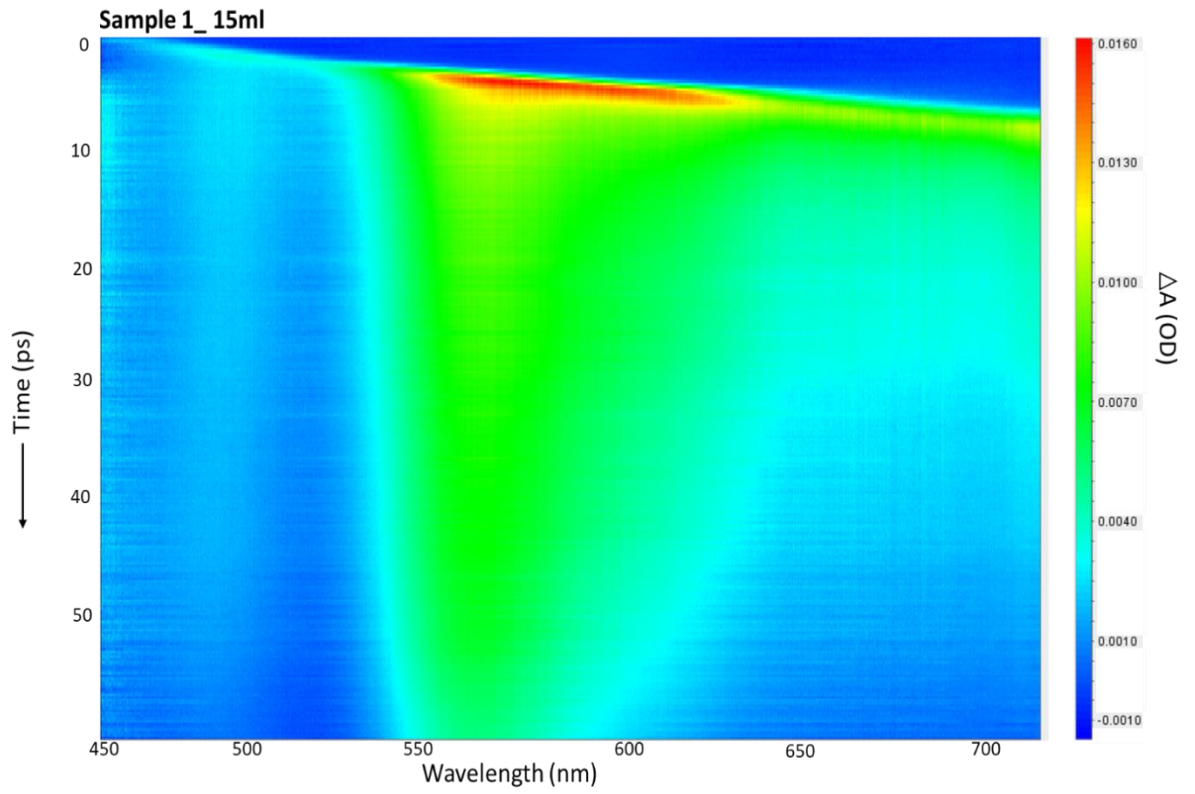

Figure 5.5. The 2-dimensional transient absorption intensity map of hematite Sample 1 prepared by spray pyrolysis with a volume of 15 ml.

5.2.1 Global analysis

To study the ultrafast carrier dynamics of hematite, we used a three-component sequential kinetic scheme by analyzing the singular value decomposition (SVD) parameters of the TA data. Each model component is characterized by an evolution associated spectrum (EAS) and associated decay lifetime (figure 5.6, a-h). In all eight of the samples an ultrafast initial component was resolved, which is attributed to the cooling of holes to the valence band maximum and electron cooling to the conduction band minimum [113]. The second decay lifetimes range between ~10 and ~20 ps and are attributed to recombination of electrons and holes as well as electron trapping by defect states and/or electronic level [114]. The third decay

lifetimes range between 320 and 854 ps and are attributed to recombination of conduction band electrons and valence band holes [113][27].

Considering only the samples prepared with 15 ml of hematite, the effect on the three decay lifetimes of three distinct parameters was investigated. In every instant, each of the individual parameters prolonged each of the lifetimes and all combinations of the three parameters enhanced this effect. Hence, there is a clear individual and cumulative effect of all three experimental parameters. The first experimental parameter was treating pristine α-Fe_2O_3 with TEOS (Sample 2), which led to a 1.2, 1.1 and 1.2 times decrease in the three recombination and other decay rates (i.e. prolongment of the lifetimes) as compared to pristine α-Fe_2O_3 (Sample 1). The TEOS chemical dopes hematite with silicon through the substitution of Fe^{3+} by Si^{4+} ions in the hematite lattice, which also results in a higher charge carrier concentration [60]. The doping of pristine hematite with Si as n-type dopant improves the photocurrent of porous films by improving charge transfer and also increases the hole diffusion length, thus prolonging the cooling of holes and electrons to the valence band maximum and conduction band minimum respectively [115][116]. Subsequently, this prolongs the recombination time of electrons and holes.

The second experimental parameter was post-annealing of pristine α-Fe_2O_3 at 500 ºC for 2 h with 10 ºC/min ramping (without TEOS treatment). We again observed a positive outcome with respect to the lifetimes. The three resolved decay rates of pristine α-Fe_2O_3 are, on average, a factor of 1.6, 1.5, and 1.3 times faster compared to those of the annealed hematite (Sample 3). The prolonged lifetime of the charge carriers suggests reduced scattering of charge carriers due to the more spherical shape with well-defined borders formed by the nanostructures [117][57]. The AFM images (figure 5.4(a-d)) confirm this, showing a reduction in the average particle size and surface roughness of Sample 3 compared to Sample 1. Since both TEOS treatment and annealing induced slower recombination rates independently, intuitively one

would expect the combination of the two treatments to reduce the recombination rates even further. Sample 4 (Table 1) was prepared by combining both TEOS treatment and post-annealing which slowed down the three excitation decay rates with a factor of ~1.8, 1.6 and 1.5, respectively, compared to those of Sample 1.

The effect of doubling the volume of hematite used in the spray pyrolysis from 15 ml to 30 ml was also investigated. This effect caused a significant reduction in the recombination and other decay rates. Specifically, the three decay rates in pristine α-Fe_2O_3 prepared by spray pyrolysis with a volume of 15 ml are on average faster by ~1.5, 1.3 and 1.8, respectively, compared to those prepared with 30 ml. This can be attributed but is not limited to the reduction in particle size with a better grain structure, as evidenced from figure 5.4 (a-h).

These results confirm that silicon-doped hematite have an improved photocurrent due to the slowing down of recombination. This suggests that elemental doping in some manner prolongs the decay lifetime of photoexcited charge carriers and therefore increases the solar to hydrogen conversion efficiency. Furthermore, the results also confirm that the annealing of hematite at certain temperatures improves the structure of the material and, as a result, reduces recombination. We also show that the use of a larger volume in spray pyrolysis can improve the crystallinity of the nanostructure and subsequently aid in slowing down recombination.

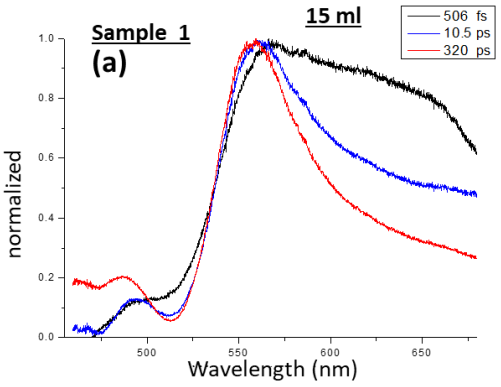
Sample 1
(a)
15 ml
506 fs
10.5 ps
320 ps
normalized
Wavelength (nm)

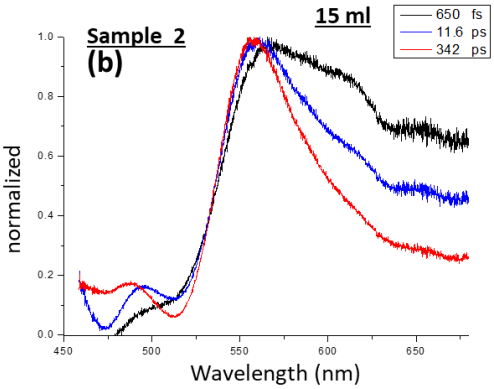
Sample 2
(b)
15 ml
650 fs
11.6 ps
342 ps
normalized
Wavelength (nm)

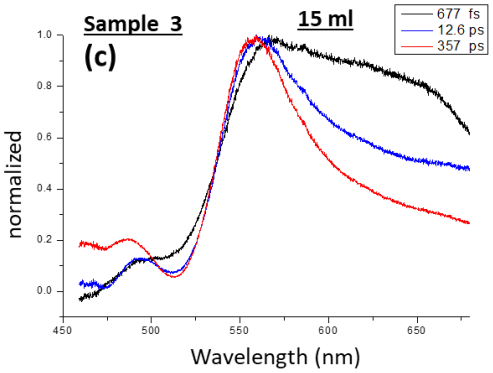
Sample 3
(c)
15 ml
677 fs
12.6 ps
357 ps
normalized
Wavelength (nm)

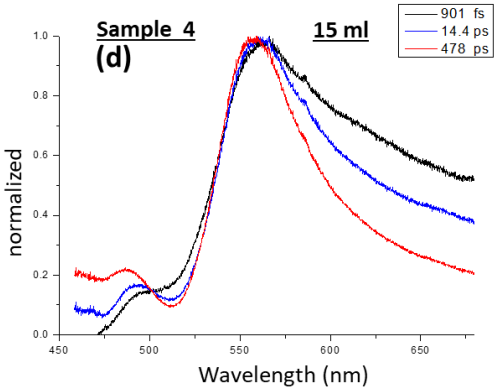
Sample 4
(d)
15 ml
901 fs
14.4 ps
478 ps
normalized
Wavelength (nm)

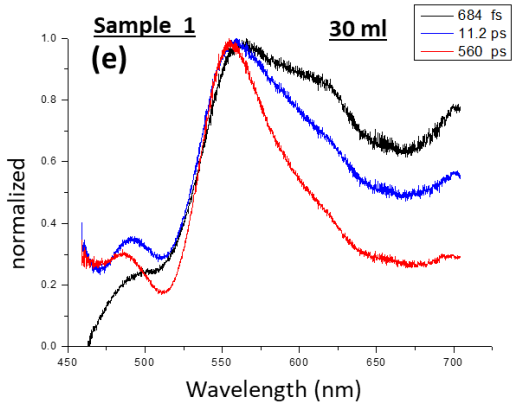
Sample 1
(e)
30 ml
684 fs
11.2 ps
560 ps
normalized
Wavelength (nm)

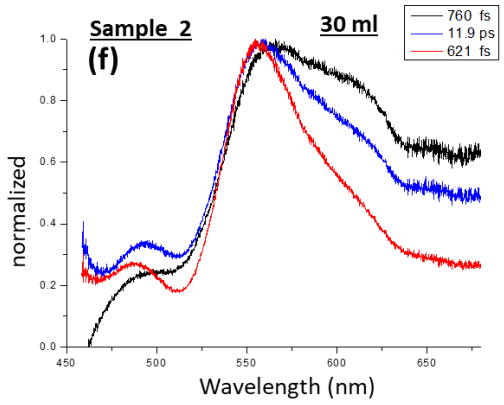
Sample 2
(f)
30 ml
760 fs
11.9 ps
621 fs
normalized
Wavelength (nm)

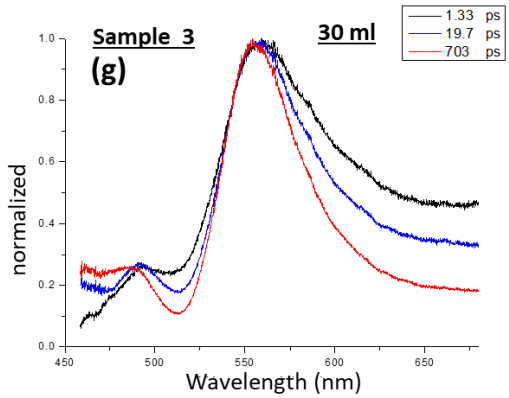
Sample 3
(g)
30 ml
1.33 ps
19.7 ps
703 ps
normalized
Wavelength (nm)

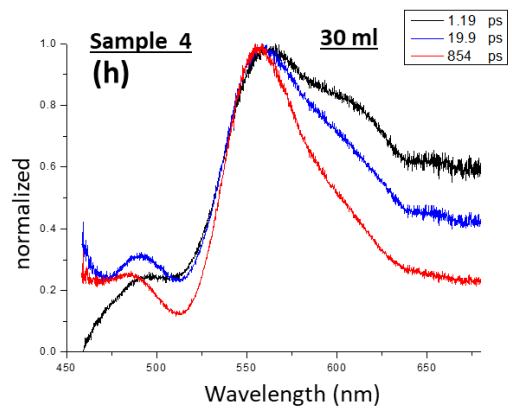
Sample 4
(h)
30 ml
1.19 ps
19.9 ps
854 ps
normalized
Wavelength (nm)

Figure 5.6. Evolution-Associated Spectra of the 8 thin film hematite samples (a-d) 15ml and (e-h) 30ml obtained after SVD analysis of the TA raw data; where the black line is the initial component, the blue line is the second component evolving from the first component and the red line is the third component evolving from the second.

Table 3. The decay lifetimes of the respective samples obtained from global analysis.

Lifetimes			
	τ_1 (fs)	**τ_2 (ps)**	**τ_3 (ps)**
Spray pyrolysis volume 15ml			
Sample 1	506	10.6	320
Sample 2	650	11.6	342
Sample 3	677	12.6	357
Sample 4	901	14.4	478
Spray pyrolysis volume 30ml			
Sample 1	684	11.2	560
Sample 2	760	11.9	622
Sample 3	1332	19.7	703
Sample 4	1192	19.9	854

Table 3 shows the decay lifetimes of the excited species within the prepared respective samples of table 2. These samples have been grouped according to the spray pyrolysis volume from which they were prepared and arranged in accordance to the different treatment i.e. the three different experimental parameters. Tau (τ) was measured in femto- and pico-seconds and the spray volume of hematite in millilitres.

CHAPTER 6

Conclusion and future work

6.1 Conclusion

In this study, eight different hematite samples were prepared by spray pyrolysis on fluorine-doped tin oxide coated glass substrates. Four were treated with TEOS and the other four were left untreated. Of these samples, four were post-annealed (two that were TEOS treated and two that were untreated) at 500 ºC for 2 hours with 10 ºC/min ramping. A high-resolution confocal Raman microscopy with an integrated atomic force microscopy was used for analysis of the hematite thin films. For all the films, Raman spectroscopy confirmed the characteristic Raman spectrum of the hematite. The high-resolution Raman mapping confirmed a uniform coating of the hematite films on the FTO substrates. In addition, the reduced surface roughness of the films seen from the Raman optical microscope images as well as atomic force microscopy surface images confirmed the uniform and conformal coverage across the FTO substrates with the average surface roughness values in the order of <10 nm. Moreover, from Raman depth profiles the thicknesses of the films were obtained and ranged between 570 and 840 nm. Ultrafast transient absorption spectroscopy was used to resolve the carrier dynamics of the thin films. Upon global analysis of the raw TA data, EAS were obtained which gave the recombination rates of the different samples. Chemical treatment of TEOS, post-annealing and increasing the spray volume led to a reduction in the recombination rates of photoexcited charge carriers on all resolved time scales, viz. 0.5-1.2 ps, 10.6-19.9 ps and 320-854 ps.

6.2 Future work

We have successfully investigated recombination rates of hematite under three experimental parameters which all gave positive results. It is widely known that photosynthesis is a naturally occurring light harvesting process that efficiently converts solar energy into useful energy through the photovoltaic effect. Therefore, the next step is to isolate a light harvesting protein from cyanobacteria that is capable of efficient light absorption like phycocyanin and study its ultrafast carrier dynamics. Thereafter, we will overlay the hematite thin film with this protein to produce a biohybrid semiconductor with enhanced chemical and optical properties.

CHAPTER 7

References

[1] "Statistical Review of World Energy | Energy economics | BP." [Online]. Available: https://www.bp.com/en/global/corporate/energy-economics/statistical-review-of-world-energy.html. [Accessed: 27-Nov-2018].

[2] "What is the greenhouse effect? – The Talking Democrat." [Online]. Available: https://www.thetalkingdemocrat.com/2018/03/what-is-the-green-house-effect/. [Accessed: 17-Jan-2019].

[3] "World Energy Scenarios 2016 report: Global energy demand growth set to fall." [Online]. Available: https://www.worldenergy.org/news-and-media/press-releases/world-energy-scenarios-2016-report-global-energy-demand-growth-set-to-fall/. [Accessed: 07-Mar-2019].

[4] A. Mohammad Bagher, "Types of Solar Cells and Application," *Am. J. Opt. Photonics*, vol. 3, no. 5, p. 94, 2015.

[5] "Earth's Energy Balance | North Carolina Climate Office." [Online]. Available: https://climate.ncsu.edu/edu/EnergyBalance. [Accessed: 17-Jan-2019].

[6] "Solar Cells - Chemistry Encyclopedia - structure, metal, equation, The pn Junction." [Online]. Available: http://www.chemistryexplained.com/Ru-Sp/Solar-Cells.html. [Accessed: 27-Nov-2018].

[7] "Photosynthesis | National Geographic Society." [Online]. Available: https://www.nationalgeographic.org/encyclopedia/photosynthesis/. [Accessed: 18-Jan-2020].

[8] “How Does a Lithium-ion Battery Work? | Department of Energy.” [Online]. Available: https://www.energy.gov/eere/articles/how-does-lithium-ion-battery-work. [Accessed: 17-Jan-2019].

[9] “The basics of lithium ion batteries – WIT Computers.” [Online]. Available: https://witcomputers.com/the-basics-of-lithium-ion-batteries/. [Accessed: 18-Jan-2020].

[10] S. Chu *et al.*, “Roadmap on solar water splitting : current status and future prospects Roadmap on solar water splitting : current status and future prospects,” 2017.

[11] F. E. Osterloh, B. A. Parkinson, and G. Editors, “Recent developments in solar water-splitting photocatalysis,” pp. 17–22, 2018.

[12] Y. J. Hwang, C. Hahn, B. Liu, and P. Yang, “Photoelectrochemical Properties of TiO_2 Nanowire Arrays: A Study of the Dependence on Length and Atomic Layer Deposition Coating,” *ACS Nano*, vol. 6, no. 6, pp. 5060–5069, Jun. 2012.

[13] T. Hisatomi, J. Kubota, and K. Domen, “Recent advances in semiconductors for photocatalytic and photoelectrochemical water splitting,” *Chem. Soc. Rev*, vol. 43, p. 7520, 2014.

[14] “Photocatalytic Water Splitting - an overview | ScienceDirect Topics.” [Online]. Available: https://www.sciencedirect.com/topics/engineering/photocatalytic-water-splitting. [Accessed: 18-Jan-2020].

[15] R. van de Krol, Y. Liang, and J. Schoonman, “Solar hydrogen production with nanostructured metal oxides,” *J. Mater. Chem.*, vol. 18, no. 20, p. 2311, May 2008.

[16] T. Hisatomi *et al.*, “Enhancement in the performance of ultrathin hematite photoanode for water splitting by an oxide underlayer,” *Adv. Mater.*, vol. 24, no. 20, pp. 2699–2702, 2012.

[17] Z. Zhou, P. Huo, L. Guo, and O. V Prezhdo, “Understanding Hematite Doping with Group IV Elements: A DFT+U Study,” 2015.

[18] J. Y. Kim *et al.*, “Single-crystalline, wormlike hematite photoanodes for efficient solar water splitting,” *Sci. Rep.*, vol. 3, no. 1, p. 2681, Dec. 2013.

[19] Z. Luo, C. Li, D. Zhang, T. Wang, and J. Gong, “Highly-oriented Fe_2O_3/$ZnFe_2O_4$ nanocolumnar heterojunction with improved charge separation for photoelectrochemical water oxidation,” *Chem. Commun.*, vol. 52, no. 58, pp. 9013–9015, Jul. 2016.

[20] “The iron oxides : structure, properties, reactions, occurrence, and uses / R.M. Cornell, U. Schwertmann. - Version details - Trove.” [Online]. Available: https://trove.nla.gov.au/work/15037099?selectedversion=NBD12586747. [Accessed: 02-Oct-2018].

[21] “Hematite: A primary ore of iron and a pigment mineral.” [Online]. Available: https://geology.com/minerals/hematite.shtml. [Accessed: 30-Jan-2019].

[22] C. Dette *et al.*, “TiO_2 Anatase with a Bandgap in the Visible Region,” *Nano Lett.*, vol. 14, no. 11, pp. 6533–6538, Nov. 2014.

[23] S. Kumari *et al.*, “Spray pyrolytically deposited nanoporous Ti4+ doped hematite thin films for efficient photoelectrochemical splitting of water,” *Int. J. Hydrogen Energy*, vol. 35, no. 9, pp. 3985–3990, 2010.

[24] L. Wang *et al.*, “Common Origin of Green Luminescence in Carbon Nanodots and Graphene Quantum Dots,” 2014.

[25] G. Nagasubramanian and A. J. Bard, “Semiconductor Electrodes,” vol. 128, no. 5, pp. 1055–1060, 1980.

[26] K. Maabong, A. G. Machatine, Y. Hu, A. Braun, F. J. Nambala, and M. Diale, “Morphology, structural and optical properties of iron oxide thin film photoanodes in photoelectrochemical cell: Effect of electrochemical oxidation,” *Phys. B Condens. Matter*, vol. 480, pp. 91–94, 2016.

[27] A. T. Paradzah, M. Diale, K. Maabong, and T. P. J. Krüger, “Use of interfacial layers to prolong hole lifetimes in hematite probed by ultrafast transient absorption spectroscopy,” 2017.

[28] V. R. Satsangi, S. Kumari, A. P. Singh, R. Shrivastav, and S. Dass, “Nanostructured hematite for photoelectrochemical generation of hydrogen,” *Int. J. Hydrogen Energy*, vol. 33, pp. 312–318, 2008.

[29] N. Beermann, L. Vayssieres, S. Lindquist, and A. Hagfeldt, “Photoelectrochemical Studies of Oriented Nanorod Thin Films of Hematite,” vol. 147, no. 7, pp. 2456–2461, 2000.

[30] P. S. Shinde, S. Y. Lee, S. H. Choi, H. H. Lee, J. Ryu, and J. S. Jang, “A Synergistic Effect of Surfactant and ZrO2 Underlayer on Photocurrent Enhancement and Cathodic Shift of Nanoporous Fe2O3 Photoanode,” *Sci. Rep.*, vol. 6, no. 1, p. 32436, Oct. 2016.

[31] S. Shen *et al.*, “Physical and photoelectrochemical properties of Zr-doped hematite nanorod arrays,” *Nanoscale*, vol. 5, no. 20, p. 9867, Sep. 2013.

[32] D. Wang *et al.*, “Uniform Doping of Titanium in Hematite Nanorods for Efficient Photoelectrochemical Water Splitting,” *ACS Appl. Mater. Interfaces*, vol. 7, no. 25, pp. 14072–14078, Jul. 2015.

[33] N. T. Hahn and C. B. Mullins, “Photoelectrochemical Performance of Nanostructured Ti- and Sn-Doped α-Fe $_2$ O $_3$ Photoanodes,” *Chem. Mater.*, vol. 22, no. 23, pp. 6474–6482, Dec. 2010.

[34] A. M. Jubb and H. C. Allen, “Vibrational spectroscopic characterization of hematite, maghemite, and magnetite thin films produced by vapor deposition,” *ACS Appl. Mater. Interfaces*, vol. 2, no. 10, pp. 2804–2812, 2010.

[35] W. Kiefer, A. P. Mazzolini, and P. R. Stoddart, “Recent Advances in linear and nonlinear Raman spectroscopy I,” *J. Raman Spectrosc.*, vol. 38, no. April, pp. 1538–1553, 2007.

[36] D. K. Bora, A. Braun, and E. C. Constable, “‘In rust we trust’. Hematite – the prospective

inorganic backbone for artificial photosynthesis," *Energy Environ. Sci.*, 2013.

[37] and B. S. Z. Y. P. He, Y. M. Miao, C. R. Li, S. Q. Wang, L. Cao, S. S. Xie, G. Z. Yang, "Size and structure effect on optical transitions of iron oxide nanocrystals."

[38] Y. Yamanoi, S. Nakashima, and M. Katsura, "Temperature dependence of reflectance spectra and color values of hematite by in situ, high-temperature visible micro-spectroscopy," *Am. Mineral.*, vol. 94, no. 1, pp. 90–97, Jan. 2009.

[39] R. M. Cornell, U. Schwertmann, and John Wiley & Sons., *The iron oxides : structure, properties, reactions, occurrences, and uses*. Wiley-VCH, 2003.

[40] S.-S. Li *et al.*, "Iron Oxide with Different Crystal Phases (α- and γ-Fe $_2$ O $_3$) in Electroanalysis and Ultrasensitive and Selective Detection of Lead(II): An Advancing Approach Using XPS and EXAFS," *Anal. Chem.*, vol. 88, no. 1, pp. 906–914, Jan. 2016.

[41] O. Zandi and T. W. Hamann, "Enhanced water splitting efficiency through selective surface state removal," *J. Phys. Chem. Lett.*, vol. 5, no. 9, pp. 1522–1526, 2014.

[42] O. Zandi, A. R. Schon, H. Hajibabaei, and T. W. Hamann, "Enhanced Charge Separation and Collection in High-Performance Electrodeposited Hematite Films," *Chem. Mater.*, vol. 28, no. 3, pp. 765–771, 2016.

[43] R. H. Misho and W. A. Murad, "Band gap measurements in thin films of hematite Fe2O3, pyrite FeS2 and troilite FeS prepared by chemical spray pyrolysis," *Sol. Energy Mater. Sol. Cells*, vol. 27, no. 4, pp. 335–345, 1992.

[44] V. R. Satsangi, S. Kumari, A. P. Singh, R. Shrivastav, and S. Dass, "Nanostructured hematite for photoelectrochemical generation of hydrogen," *Int. J. Hydrogen Energy*, vol. 33, no. 1, pp. 312–318, 2008.

[45] A. Duret and M. Grätzel, "Visible light-induced water oxidation on mesoscopic α-Fe 2O3 films

made by ultrasonic spray pyrolysis," *J. Phys. Chem. B*, vol. 109, no. 36, pp. 17184–17191, 2005.

[46] S. Bagheri, C. K. G, and S. Bee Abd Hamid, "Generation of Hematite Nanoparticles via Sol-Gel Method," 2013.

[47] K. G. Chandrappa, T. V. Venkatesha, K. Vathsala, and C. Shivakumara, "A hybrid electrochemical–thermal method for the preparation of large ZnO nanoparticles," *J. Nanoparticle Res.*, vol. 12, no. 7, pp. 2667–2678, Sep. 2010.

[48] G. S. Li, R. L. Smith, H. Inomata, and K. Arai, "Preparation and magnetization of hematite nanocrystals with amorphous iron oxide layers by hydrothermal conditions," *Mater. Res. Bull.*, vol. 37, no. 5, pp. 949–955, Apr. 2002.

[49] X. Hu, J. C. Yu, and J. Gong, "Fast Production of Self-Assembled Hierarchical r-Fe 2 O 3 Nanoarchitectures," 2007.

[50] M. Cao *et al.*, "Single-Crystal Dendritic Micro-Pines of Magnetic α-Fe2O3: Large-Scale Synthesis, Formation Mechanism, and Properties," *Angew. Chemie*, vol. 117, no. 27, pp. 4269–4273, Jul. 2005.

[51] G. Wang *et al.*, "Facile Synthesis of Highly Photoactive α-Fe $_2$ O $_3$ -Based Films for Water Oxidation," *Nano Lett.*, vol. 11, no. 8, pp. 3503–3509, Aug. 2011.

[52] M. B. Sahana *et al.*, "Bandgap engineering by tuning particle size and crystallinity of SnO2–Fe2O3 nanocrystalline composite thin films," *Appl. Phys. Lett.*, vol. 93, no. 23, p. 231909, Dec. 2008.

[53] J. M. Electrochemical Society., R. Shinar, and J. P. Ziegler, *Journal of the Electrochemical Society.*, vol. 127. Electrochemical Society, 1948.

[54] T. Hisatomi *et al.*, "Cathodic shift in onset potential of solar oxygen evolution on hematite by

13-group oxide overlayers," *Energy Environ. Sci.*, vol. 4, no. 7, p. 2512, Jul. 2011.

[55] P. S. Shinde, S. Y. Lee, S. H. Choi, H. H. Lee, J. Ryu, and J. S. Jang, "A Synergistic Effect of Surfactant and ZrO2 Underlayer on Photocurrent Enhancement and Cathodic Shift of Nanoporous Fe2O3 Photoanode," *Sci. Rep.*, vol. 6, no. 1, p. 32436, Oct. 2016.

[56] M. J. Kang and Y. S. Kang, "Ultrathin insulating under-layer with a hematite thin film for enhanced photoelectrochemical (PEC) water splitting activity," *J. Mater. Chem. A*, vol. 3, no. 30, pp. 15723–15728, Jul. 2015.

[57] J. Y. Kim *et al.*, "Single-crystalline, wormlike hematite photoanodes for efficient solar water splitting," *Sci. Rep.*, vol. 3, no. 1, p. 2681, Dec. 2013.

[58] R. F. G. Gardner, F. Sweett, and D. W. Tanner, "The electrical properties of alpha ferric oxide—II.: Ferric oxide of high purity," *J. Phys. Chem. Solids*, vol. 24, no. 10, pp. 1183–1196, Oct. 1963.

[59] "Fundamentals of Semiconductor physics - Insulator, semiconductor, conductor." [Online]. Available: http://www.optique-ingenieur.org/en/courses/OPI_ang_M05_C02/co/Contenu_02.html. [Accessed: 18-Jan-2020].

[60] I. Cesar, A. Kay, J. A. Gonzalez Martinez, and M. Grä, "Translucent Thin Film Fe 2 O 3 Photoanodes for Efficient Water Splitting by Sunlight: Nanostructure-Directing Effect of Si-Doping," *J. AM. CHEM. SOC*, vol. 128, pp. 4582–4583, 2006.

[61] M. H. N. Assadi and D. A. H. Hanaor, "Theoretical study on copper's energetics and magnetism in TiO2 polymorphs," Apr. 2013.

[62] A. B. Sproul and M. A. Green, "Improved value for the silicon intrinsic carrier concentration from 275 to 375 K," *J. Appl. Phys.*, vol. 70, no. 2, pp. 846–854, 1991.

[63] B. Ohtani, "PHOTOCATALYSIS BY INORGANIC SOLID MATERIALS: REVISITING ITS DEFINITION,

CONCEPTS, AND EXPERIMENTAL PROCEDURES."

[64] "Silicon and Germanium." [Online]. Available: http://hyperphysics.phy-astr.gsu.edu/hbase/Solids/sili.html. [Accessed: 30-Jan-2019].

[65] "What is Drift Current : Its Relation with Drift Velocity & Density." [Online]. Available: https://www.watelectronics.com/drift-current-relation-with-velocity/. [Accessed: 18-Jan-2020].

[66] J. Y. Kim *et al.*, "Single-crystalline, wormlike hematite photoanodes for efficient solar water splitting," *Sci. Rep.*, vol. 3, Sep. 2013.

[67] O. Neufeld and M. C. Toroker, "Platinum-doped α-Fe2O3 for enhanced water splitting efficiency: A DFT+ U study," *J. Phys. Chem. C*, vol. 119, no. 11, pp. 5836–5847, Mar. 2015.

[68] S. Shen *et al.*, "Physical and photoelectrochemical properties of Zr-doped hematite nanorod arrays," *Nanoscale*, vol. 5, no. 20, pp. 9867–9874, Oct. 2013.

[69] A. Annamalai *et al.*, "Sn/Be Sequentially co-doped Hematite Photoanodes for Enhanced Photoelectrochemical Water Oxidation: Effect of Be2+ as co-dopant," *Sci. Rep.*, vol. 6, Mar. 2016.

[70] P. S. Shinde, S. H. Choi, Y. Kim, J. Ryu, and J. S. Jang, "Onset potential behavior in α-Fe2O3 photoanodes: the influence of surface and diffusion Sn doping on the surface states," *Phys. Chem. Chem. Phys.*, vol. 18, no. 4, pp. 2495–2509, Jan. 2016.

[71] C. X. Kronawitter *et al.*, "Titanium incorporation into hematite photoelectrodes: Theoretical considerations and experimental observations," *Energy and Environmental Science*, vol. 7, no. 10. Royal Society of Chemistry, pp. 3100–3121, 01-Oct-2014.

[72] O. Zandi, B. M. Klahr, and T. W. Hamann, "Highly photoactive Ti-doped ??-Fe<inf>2</inf>O<inf>3</inf> thin film electrodes: Resurrection of the dead layer," *Energy*

Environ. Sci., vol. 6, no. 2, pp. 634–642, 2013.

[73] F. J. Morin, "Electrical properties of αfe2O3 and αfe2O3 containing titanium," *Phys. Rev.*, vol. 83, no. 5, pp. 1005–1010, 1951.

[74] G. Wang *et al.*, "Facile synthesis of highly photoactive α-Fe2O 3-based films for water oxidation," *Nano Lett.*, vol. 11, no. 8, pp. 3503–3509, Aug. 2011.

[75] W. B. Ingler and S. U. M. Khan, "Photoresponse of spray pyrolytically synthesized copper-doped p-Fe 2O3 thin film electrodes in water splitting," *Int. J. Hydrogen Energy*, vol. 30, no. 8, pp. 821–827, Jul. 2005.

[76] S. Shen *et al.*, "Surface engineered doping of hematite nanorod arrays for improved photoelectrochemical water splitting," *Sci. Rep.*, vol. 4, 2014.

[77] W. B. Ingler and S. U. M. Khan, "A self-driven pn- Fe2 O3 tandem photoelectrochemical cell for water splitting," *Electrochem. Solid-State Lett.*, vol. 9, no. 4, 2006.

[78] J. H. Kim *et al.*, "Awakening solar water-splitting activity of ZnFe2O4 nanorods by hybrid microwave annealing," *Adv. Energy Mater.*, vol. 5, no. 6, Mar. 2015.

[79] N. Mirbagheri *et al.*, "Visible light driven photoelectrochemical water oxidation by Zn- and Ti-doped hematite nanostructures," *ACS Catal.*, vol. 4, no. 6, pp. 2006–2015, Jun. 2014.

[80] X. Qi, G. She, M. Wang, L. Mu, and W. Shi, "Electrochemical synthesis of p-type Zn-doped α-Fe 2 O 3 nanotube arrays for photoelectrochemical water splitting," *Chem. Commun.*, vol. 49, no. 51, pp. 5742–5744, Jun. 2013.

[81] Z. Fan, X. Wen, S. Yang, and J. G. Lu, "Controlled p- and n-type doping of Fe 2O 3 nanobelt field effect transistors," *Appl. Phys. Lett.*, vol. 87, no. 1, Jul. 2005.

[82] Y. Hou, F. Zuo, A. Dagg, and P. Feng, "A three-dimensional branched cobalt-doped α-Fe2O 3 nanorod/MgFe2O4 heterojunction array as a flexible photoanode for efficient

photoelectrochemical water oxidation," *Angew. Chemie - Int. Ed.*, vol. 52, no. 4, pp. 1248–1252, Jan. 2013.

[83] Y. Lin *et al.*, "Growth of p-type hematite by atomic layer deposition and its utilization for improved solar water splitting," *J. Am. Chem. Soc.*, vol. 134, no. 12, pp. 5508–5511, Mar. 2012.

[84] W. D. Chemelewski, N. T. Hahn, and C. B. Mullins, "EFFECT of Si doping and porosity on hematite's (α-Fe 2O 3) photoelectrochemical water oxidation performance," *J. Phys. Chem. C*, vol. 116, no. 8, pp. 5255–5261, Mar. 2012.

[85] X. Zhao *et al.*, "The Influence of Ti Doping on Morphology and Photoelectrochemical Properties of Hematite Grown from Aqueous Solution for Water Splitting," *Energy Technol.*, vol. 6, no. 11, pp. 2188–2199, Nov. 2018.

[86] X. Y. Meng *et al.*, "Enhanced photoelectrochemical activity for Cu and Ti doped hematite: The first principles calculations," *Appl. Phys. Lett.*, vol. 98, no. 11, Mar. 2011.

[87] "C.V. Raman The Raman Effect - Landmark - American Chemical Society." [Online]. Available: https://www.acs.org/content/acs/en/education/whatischemistry/landmarks/ramaneffect.html. [Accessed: 18-Jan-2020].

[88] "The rise of Raman - European Pharmaceutical Review." [Online]. Available: https://www.europeanpharmaceuticalreview.com/article/3018/the-rise-of-raman/. [Accessed: 18-Jan-2020].

[89] I. Galván and A. Jorge, "Dispersive Raman spectroscopy allows the identification and quantification of melanin types," *Ecol. Evol.*, vol. 5, no. 7, pp. 1425–1431, Apr. 2015.

[90] D. J. Gardiner, "Introduction to Raman Scattering," in *Practical Raman Spectroscopy*, Berlin, Heidelberg: Springer Berlin Heidelberg, 1989, pp. 1–12.

[91] “1: (a) Schematic diagram of light scattering by Rayleigh, Stokes and... | Download Scientific Diagram.” [Online]. Available: https://www.researchgate.net/figure/a-Schematic-diagram-of-light-scattering-by-Rayleigh-Stokes-and-Anti-Stokes_fig3_305386684. [Accessed: 18-Jan-2020].

[92] T. Thompson, “Fundamentals of Raman spectroscopy.”

[93] D. C. Harris and M. D. Bertolucci, *Symmetry and spectroscopy : an introduction to vibrational and electronic spectroscopy*. Dover Publications, 1989.

[94] K. J. I. Ember *et al.*, “Raman spectroscopy and regenerative medicine: a review,” *npj Regen. Med.*, vol. 2, no. 1, p. 12, Dec. 2017.

[95] “From Disorder to Order: The Functional Flexibility of Single Plant Light-Harvesting Complexes — Vrije Universiteit Amsterdam.” [Online]. Available: https://research.vu.nl/en/publications/from-disorder-to-order-the-functional-flexibility-of-single-plant. [Accessed: 18-Jan-2020].

[96] P. Davidovits and M. D. Egger, “Scanning laser microscope,” *Nature*, vol. 223, no. 5208. p. 831, 1969.

[97] “Atomic Force Microscopy (AFM) in a Scanning Electron Microscope (SEM) for Nanomaterials Research.” [Online]. Available: https://www.zeiss.com/microscopy/int/cmp/mat/20/nanomaterials/afmsem/afm-for-nanomaterials.html?utm_source=googleppc&utm_medium=search&utm_campaign=afm-sem-nanomaterials-2020&gclid=Cj0KCQiA9orxBRD0ARIsAK9JDxTtS06k3VwLMATKI8z1Ehwheg5NlMsmC-DpIvO8O6Yuqxg64BDEbhYaAgT4EALw_wcB. [Accessed: 18-Jan-2020].

[98] O. Kühn and S. Lochbrunner, “Ultrafast Spectroscopy,” in *digital Encyclopedia of Applied Physics*, Weinheim, Germany: Wiley-VCH Verlag GmbH & Co. KGaA, 2009, pp. 769–815.

[99] H. He, W. Li, X. Zhang, M. Xia, and K. Yang, “Light scattering by a spheroidal bubble with geometrical optics approximation,” *J. Quant. Spectrosc. Radiat. Transf.*, vol. 113, no. 12, pp. 1467–1475, Aug. 2012.

[100] D. M. Niedzwiedzki, M. M. Enriquez, A. M. Lafountain, and H. A. Frank, “Ultrafast time-resolved absorption spectroscopy of geometric isomers of xanthophylls,” *Chem. Phys.*, vol. 373, no. 1–2, pp. 80–89, Jul. 2010.

[101] R. Berera, R. van Grondelle, and J. T. M. Kennis, “Ultrafast transient absorption spectroscopy: principles and application to photosynthetic systems,” *Photosynth. Res.*, vol. 101, no. 2–3, pp. 105–118, Sep. 2009.

[102] “FEMTOSECOND PUMP -PROBE SYSTEM ExciPro User’s Manual.”

[103] $ Ivo, H. M. Van Stokkum, D. S. Larsen, and R. Van Grondelle, “Global and target analysis of time-resolved spectra.”

[104] J. Snellenburg, S. Laptenok, R. Seger, K. Mullen, and I. Van Stokkum, “Glotaran: A Java-based graphical user interface for the R package TIMP,” *J. Stat. Softw.*, vol. 49, no. 3, p. , 2011.

[105] R. Thiagarajan, M. Anusuya, and M. M. Beevi, “Mechanical Characterization of Spray Pyrolytic Cadmium Sulphide Thin Films by Indentation Technique,” vol. 5, no. 6, pp. 51–56, 2009.

[106] A. G. Joly, J. R. Williams, S. A. Chambers, G. Xiong, W. P. Hess, and D. M. Laman, “Carrier dynamics in (0001) thin films and single crystals probed by femtosecond transient absorption and reflectivity,” *Cit. J. Appl. Phys.*, vol. 99, p. 144305, 2006.

[107] D. Bersani, P. P. Lottici, and X.-Z. Ding, “Phonon confinement effects in the Raman scattering by TiO2 nanocrystals,” *Appl. Phys. Lett.*, vol. 72, no. 1, p. 73, Jun. 1998.

[108] G. P. Demopoulos, C. Charbonneau, K. Lee, G. Shan, M. A. Gomez, and R. Gauvin, “Synthesis of Hydroxyl-Rich Anatase Nanocrystallites, Their Characterization and Performance as

Photoanode in Dye-Sensitized Solar Cells," in *ECS Transactions*, 2009, vol. 21, no. 1, pp. 23–34.

[109] S. K. Gupta, R. Desai, P. K. Jha, S. Sahoo, and D. Kirin, "Titanium dioxide synthesized using titanium chloride: size effect study using Raman spectroscopy and photoluminescence," *J. Raman Spectrosc.*, vol. 41, no. 3, p. n/a-n/a, Mar. 2009.

[110] S. Balaji, Y. Djaoued, and J. Robichaud, "Phonon confinement studies in nanocrystalline anatase-TiO2 thin films by micro Raman spectroscopy," *J. Raman Spectrosc.*, vol. 37, no. 12, pp. 1416–1422, Dec. 2006.

[111] S. R. Pendlebury *et al.*, "Dynamics of photogenerated holes in nanocrystalline α-Fe 2O3 electrodes for water oxidation probed by transient absorption spectroscopy," *Chem. Commun.*, vol. 47, no. 2, pp. 716–718, Jan. 2011.

[112] Z. Huang *et al.*, "In situ probe of photocarrier dynamics in water-splitting hematite (α-Fe2O3) electrodes," *Energy Environ. Sci.*, vol. 5, no. 10, p. 8923, Sep. 2012.

[113] A. G. Joly, J. R. Williams, S. A. Chambers, G. Xiong, W. P. Hess, and D. M. Laman, "Carrier dynamics in α-Fe2O3 (0001) thin films and single crystals probed by femtosecond transient absorption and reflectivity," *J. Appl. Phys.*, vol. 99, no. 5, p. 053521, Mar. 2006.

[114] N. J. Cherepy, D. B. Liston, J. A. Lovejoy, H. Deng, and J. Z. Zhang, "Ultrafast studies of photoexcited electron dynamics in γ- and α-Fe2O3 semiconductor nanoparticles," *J. Phys. Chem. B*, vol. 102, no. 5, pp. 770–776, Jan. 1998.

[115] I. Cesar, K. Sivula, A. Kay, R. Zboril, and M. Grätzel, "Influence of Feature Size, Film Thickness, and Silicon Doping on the Performance of Nanostructured Hematite Photoanodes for Solar Water Splitting," *J. Phys. Chem. C*, vol. 113, no. 2, pp. 772–782, Jan. 2009.

[116] W. D. Chemelewski, N. T. Hahn, and C. B. Mullins, "Effect of Si Doping and Porosity on Hematite's (α-Fe $_2$ O $_3$) Photoelectrochemical Water Oxidation Performance," *J. Phys. Chem.*

C, vol. 116, no. 8, pp. 5255–5261, Mar. 2012.

[117] “Annealing effects on structural and magnetic properties of α-Fe2O3 nanoparticles,” *J. Magn. Magn. Mater.*, vol. 226–230, pp. 1907–1909, May 2001.